JM PAPERS

Cross-wind-induced spanwise flapping of tandem turbulent diffusion flames: experimental- and large eddy simulation-based study

Yuhang Chen[1,†], Kazui Fukumoto[1,†] ⓘD, Yanli Miao[1], Jingru Zheng[1], Fei Tang[1] ⓘD and Longhua Hu[1] ⓘD

[1]State Key Laboratory of Fire Science, University of Science and Technology of China, Hefei, Anhui 230026, PR China
Corresponding authors: Longhua Hu, hlh@ustc.edu.cn; Fei Tang, ftang@ustc.edu.cn

This research investigates the spanwise oscillation patterns of turbulent non-premixed flames in a tandem configuration, using both experimental methods and large eddy simulations under cross-airflow conditions. Based on the heat release rate (17.43–34.86 kW) and the burner size (0.15 × 0.15 m), the flame behaves like both a buoyancy-controlled fire (such as a pool fire) and, due to cross-wind effects, a forced flow-controlled fire. The underlying fire dynamics was modelled by varying the spacing between the square diffusion burners, cross-wind velocity and heat release rate. Two flapping modes, the oscillating and bifurcating modes, were observed in the wake of the downstream diffusion flame. This behaviour depends on the wake of the upstream diffusion flame. As the backflow of the upstream flame moved downstream, the maximum flame width of the downstream flame became broader. The flapping amplitude decreased with a stronger cross-wind. Furthermore, the computational fluid dynamics simulation was performed by FireFOAM based on OpenFOAM v2006 2020 to investigate the flapping mechanism. The simulation captured both modes well. Disagreement of the flapping period on the left and right sides results in the oscillating mode, while an agreement of the flapping period results in the bifurcating mode. Finally, the scaling law expressed the dimensionless maximum flame width with the proposed set of basic dimensional parameters, following observations and interpretation by simulations. The results help prevent the potential hazards of this type of basic fire scenario and are fundamentally significant for studying wind-induced multiple fires.

Key words: vortex shedding, flames, wakes

[†]Both authors contributed equally as co-first authors.

Y. Chen, K. Fukumoto, Y. Miao, J. Zheng, F. Tang and L. Hu

1. Introduction

When a fire occurs in a densely populated area with a high concentration of houses or office buildings, such as an urban setting, the flames may spread to nearby buildings. Interactions among multiple fires nearby are potential risks, leading to devastating mass fires or even more disastrous hazards in wildland or urban areas (Harris & McDonald 2022). Thus, basic knowledge and prediction regarding the interaction of multiple fires is crucial in minimising the impacts and risks of fires. From a fluid mechanics perspective, the interaction of multiple fires results from the interference of the surrounding flow field due to other nearby fires. These fires restrict the air entrainment process and then lead to a change in flame geometry and the burning rate (Chen *et al.* 2023*a*). In this regard, understanding the intrinsic physics of multiple fire interactions and burning behaviour in wind-free conditions has been extensively investigated, such as investigating flame merging dynamics and flame height (Baldwin 1968; Maynard, Princevac & Weise 2016). Buoyant turbulent fires can be deemed sinks because of the pressure drop, drawing in and engulfing the surrounding air to sustain combustion. The drawing in the airflow of fires interacts with the other nearby fires, causing the flame to merge or converge. Trelles & Pagni (1991) reported that the horizontal fire-induced airflow was drawn towards the centroid of multiple fires in the Oakland Hills fire. Many relevant works have been comprehensively summarised in a number of review articles (Vasanth *et al.* 2014; Liu *et al.* 2021; Chen *et al.* 2023*a*). However, in real fire scenarios, the absence of wind is considered an ideal condition, and field-based findings should account for the effects of cross-winds. Under the effect of heat and flow fields, an interaction among multiple fires becomes more complex. Several scholars have investigated the flame interaction dynamics and burning behaviours of multiple fires to clarify the multiple fire behaviours in the wind. Note that two flames under wind, the basic components of multiple fires, become the focus of research interest.

Morvan *et al.* (2011) performed two- and three-dimensional wildfire simulations with two fire sources and different fuel compositions. They concluded that the results reasonably reproduced the front and trailing edge interaction. However, they also suggested that further research is needed to improve the accuracy. Rather recently, Chen *et al.* (2021), Li *et al.* (2021) and Tang *et al.* (2023) experimentally studied the flame–flame interaction of tandem turbulent diffusion flames. The results indicated that flames were more likely to merge under a cross-wind inertial force. The tilt angle of the downstream flames was observed to be smaller than that of the upstream ones, a phenomenon attributed to the blockage effect caused by the upstream fire. This effect significantly alters the flow impinging on the downstream flame, making it considerably different from the free stream. Furthermore, a diffusion flame can be deemed a deformable object, which presents some features in contrast to a rigid body immersed in a fluid stream owing to the unsteady interaction between the hydrodynamics and inertia (Shelley & Zhang 2011). A group of deformable bodies moving through a viscous incompressible flowing fluid is a ubiquitous issue in nature, of which the scenario of multiple flapping flags interacting with a cross-wind has been actively investigated as an archetype (Ristroph & Zhang 2008). When the incoming airflow passes around the objects, hydrodynamic forces will change the shape of these bodies (i.e. morphological characteristics). In turn, the shape-changed flexible bodies also modify the surrounding hydrodynamic forces, and these strongly coupled effects make it a challenge to understand this problem fully. Ristroph & Zhang (2008) experimentally investigated the hydrodynamic drafting of a tandem pair of interacting flapping flags with varied gaps. They found that they undulate in a downwind flowing soap film with greater lateral amplitudes for the follower than the leader. Zhu (2009) and

Uddin, Huang & Sung (2015) performed numerical simulations on the interaction of a pair of tandem flexible flags separated in a flowing viscous incompressible fluid at various Reynolds numbers.

Similar to a flapping flag, a diffusion flame can also be seen as a flexible hot fluid that undulates under airflow. What will happen when dual tandem fires are subjected to the cross-airflow? Inspired by the undulation phenomenon of a pair of tandem flexible, shape-changing objects in a two-dimensional plane under a cross-wind, we first explore this kind of problem for two nearby fires, a case which is commonly seen in practical fire accidents (Finney & McAllister 2011). This unexplored potential flame flapping that might ignite neighbouring combustibles is of great practical interest, which is very important in wildland fires or tank fires in refineries. The interaction of flame–flame in tandem arrangement in the presence of wind is a complex three-dimensional flame–flow dynamics problem. Although these data are reported for two flame geometries in the streamwise direction (Chen *et al.* 2021), how the two tandem diffusion flames interact in the spanwise direction remains unknown, posing a really interesting question. However, few reports on the flame interaction are as yet available in the spanwise direction.

This study focused on the movement of flames seen from an overhead view, and we discovered a peculiar phenomenon induced by the movement of flames in the spanwise direction. The authors named these fire motions the oscillating mode, in which the flame oscillates from side to side as a single mass, and the bifurcating mode, in which the flame splits into two large parts. From a fire safety standpoint, the bifurcating mode indicates the possibility of flames spreading to more distant houses because flames spread to both sides. From a fluid dynamics point of view, it would be interesting to investigate why flames of such shapes appear alternately.

Three main contents were included in this study. A series of experiments was performed to investigate the flame–flame interaction and morphological characteristics in the spanwise direction, using two square gaseous burners with various heat release rates and separation distances in a wind tunnel. The flame motion phenomenon in the spanwise direction was observed, discussed and interpreted experimentally. In the second part, the flame motion was reproduced using computational fluid dynamics (CFD) simulation based on large eddy simulation (LES) to explain the mechanism of the two modes. Finally, the maximum flame width was modelled through the scaling analysis.

2. Methods

2.1. *Experimental set-up*

Figure 1 presents a schematic diagram of the experimental set-up. It comprises a wind tunnel, two gaseous diffusion burners, mass flow controllers and a sampling system. The dimensions of the wind tunnel are 1.5 m high and 1.3 m wide. The cross-wind generated by the wind tunnel ranges from 0 to 3.0 m s^{-1} with a local turbulence intensity of less than 5 %, monitored by four-probe hot-wire anemometers (accuracy: ± 0.01 m s^{-1}) in real time. The two identical square stainless-steel gas burners included a quartz sand layer of 10 cm and a side length of 15 cm in the tandem arrangement. A 40 cm thin fireproofing panel was placed between the wind tunnel exit and the leading edge of the first burner to minimise the bluff body effect and avoid flow separation at the leading edge of the burner. The position of the first burner was fixed, and the separation distance (S) between these two burners was altered by moving the downstream burner farther away. The velocity boundary profile upstream of the first burners is measured and presented in figure 1. As fuel, C$_3$H$_8$ was used to sustain stable total heat release rates ($\dot{Q}$), controlled by fuel
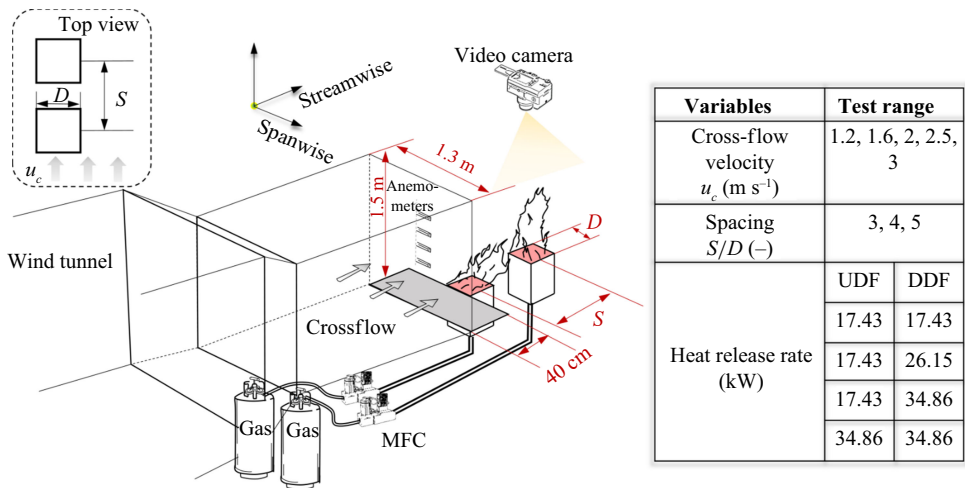
Figure 1. Schematic of the experimental set-up.

supply rates. Gas mass flow issuing from each burner was controlled by one mass flow controller with the accuracy of 0.1 SLPM (standard litre per minute). The heat release rate of both the upstream diffusion flame (UDF) and the downstream diffusion flame (DDF) was regulated, ranging from 17.43 to 34.86 kW. Both equal and unequal heat release rates for these two burners were considered. An overhead video camera at 25 frames per second and a resolution of 1920×1080 pixels captured the burning process in the spanwise direction. Flame maximum width (W) in the spanwise direction was determined using the intermittency distribution contour ($I = 0.05$) by averaging all recorded images (Chen *et al.* 2021). In contrast to the two-dimensional problem of two flags in a cross-wind, when two flames are close, they interact due to the pressure drop caused by air entrainment, even in still air, making the observation and investigation of this problem more complex. In order to exclude the effect of pressure thrust caused by the entrained air, we mainly focus on the mutual influences between flames that are dominated by cross-wind ($S/D = 3, 4,$ and 5) in this work. Beyond that, because two flames will fully merge and act just like one equivalent flame, trailing fire may hinder the flapping motion of the leading fire (Chen *et al.* 2021). Besides, one could not tell the behaviour of each diffusion flame and their interaction under cross-wind. This study pays attention to cases when flames are not fully merging. The cases under cross-wind velocities from 1.2 to 3.0 m s^{-1} with separation distances (S/D) from 3 to 5 are considered in this work based on the results of preliminary tests and previous research. Seventy-five tests were conducted, including reference tests with an isolated diffusion flame (IDF). Each test was repeated at least three times, showing good repeatability for the following analysis. Error bars in the figure mean the standard deviation of the maximum flame width.

2.2. *Mathematical models*

This study utilises the LES-based FireFOAM solver, which is an in-house version of the authors' group. Previous studies provided information about the modifications made regarding the examination of various fire scenarios, such as flame spread on solid fuels (Fukumoto, Wang & Wen 2018), syngas jet flames (Fukumoto, Wang & Wen 2019) and pool fires incorporating liquid fuel flows (Fukumoto *et al.* 2020). The difference from the standard version is that diffusion coefficients can be set for each chemical species. The dynamic Smagorinsky model (Germano *et al.* 1991; Lilly 1992) for a turbulence model

is available. The combustion model used is the eddy dissipation model based on the energy cascade concept for the LES (Chen *et al.* 2014), and the weighted sum of the grey gases model (Smith, Shen & Frledman 1982) is incorporated as a radiation model.

2.2.1. *Governing equations*

The FireFOAM solver solves the continuity, momentum, mass fraction of chemical species J and sensible enthalpy equations. The coupling algorithm for the momentum and continuity equations is known as pressure-implicit with splitting of operators, including the outer iteration. The algorithm is referred to as PIMPLE (a combined PISO–SIMPLE algorithm, where PISO stands for Pressure-Implicit with Splitting of Operators and SIMPLE stands for Semi-Implicit Method for Pressure-Linked Equations; implemented in OpenFOAM v2006 (2020)). For PIMPLE parameters, the number of outer iterations is 3, and the number of the pressure-corrector iterations is 3. The respective equations are as follows:

Continuity equation

$$\frac{\partial \bar{\rho}}{\partial t} + \frac{\partial \bar{\rho} \tilde{u}_i}{\partial x_i} = 0. \tag{2.1}$$

Momentum equation

$$\frac{\partial \bar{\rho} \tilde{u}_i}{\partial t} + \frac{\partial \bar{\rho} \tilde{u}_i \tilde{u}_j}{\partial x_i} = \frac{\partial}{\partial x_i} \left[(\mu + \mu_{SGS}) \left(\frac{\partial \tilde{u}_j}{\partial x_i} + \frac{\partial \tilde{u}_i}{\partial x_j} - \frac{2}{3} \frac{\partial \tilde{u}_k}{x_k} \delta_{ij} \right) \right] - \frac{\partial \bar{p}_{rgh}}{\partial x_i} - g_j x_j \frac{\partial \bar{\rho}}{\partial x_i}, \tag{2.2}$$

$$\bar{p}_{rgh} = \bar{p} - \bar{\rho} g_j x_j. \tag{2.3}$$

Mass fraction equation of gas species J

$$\frac{\partial \bar{\rho} \tilde{Y}_J}{\partial t} + \frac{\partial \bar{\rho} \tilde{u}_i \tilde{Y}_J}{\partial x_i} = \frac{\partial}{\partial x_i} \left[\left(\frac{\mu_{SGS}}{Sc_t} \frac{\partial \tilde{Y}_J}{\partial x_i} \right) - j_{iJ} \right] + \bar{\omega}_J. \tag{2.4}$$

Sensible enthalpy equation

$$\frac{\partial \bar{\rho} \tilde{h}}{\partial t} + \frac{\partial \bar{\rho} \tilde{u}_i \tilde{h}}{\partial x_i} = \frac{D\bar{p}}{Dt} + \frac{\partial}{\partial x_i} \left[\left(\bar{\rho} D_h + \frac{\mu_{SGS}}{Pr_t} \right) \frac{\partial \tilde{h}}{\partial x_i} \right] - \sum_J j_{iJ} h_J + q'''_{reac} - \nabla \cdot q''_{rad}, \tag{2.5}$$

where $^-$ is the time average, $^\sim$ is the density-weighted average, $\bar{\rho}$ is the density (kg m^{-3}), t is the time (s), u_j is the velocity in the j direction (m s^{-1}), x_j is the coordinate in the j direction (m), μ is the dynamic viscosity (Pa·s), μ_{SGS} is the sub-grid-scale viscosity (Pa·s), $\bar{p}_{rgh}$ is the modified pressure (Pa), $\bar{p}$ is the static pressure (Pa), g_j is the gravitational acceleration in the j direction (m s^{-2}), $\tilde{Y}_J$ is the mass fraction of chemical species J, Sc_t is the turbulent Schmidt number ($= 0.85$, a default value was used), j_{iJ} is the mass diffusion flux (kg (m^{-2}·s^{-1})), $\bar{\omega}_J$ is the reaction rate of chemical species J (kg (m^{-3}·s^{-1})), $\tilde{h}$ is the sensible enthalpy (J kg^{-1}), D_h is the thermal diffusivity (m^2 s^{-1}), Pr_t is the turbulent Prandtl number ($= 0.85$, a default value was used), q'''_{reac} is the volumetric heat release rate due to reaction (W m^{-3}) and q''_{rad} is the radiative heat flux (W m^{-2}). Equation (2.2) includes p_{rgh}, which is the static pressure minus the potential energy, to account for the effect of buoyancy by the last term. For the discretisation scheme, the second-order 'filteredLinear2V' scheme is used for the momentum equation, and the second-order

'limitedLinear' scheme is used for the mass fraction and enthalpy equations (OpenFOAM v2006 2020).

The parameter j_{iJ} is calculated as

$$j_{iJ} = -\bar{\rho} D_{diff,J} \frac{\partial \tilde{Y}_J}{\partial x_i} - \frac{D_J^T \Delta \tilde{T}}{\tilde{T}}, \tag{2.6}$$

where $\tilde{T}$ is the temperature and the thermal diffusivity D_h is modelled by

$$D_h = \frac{\kappa}{C_p \bar{\rho}}, \tag{2.7}$$

where C_p is the heat capacity at the constant pressure ($J\,(kg^{-1}{\cdot}K^{-1})$), and $D_{diff,J} = D_h/Le_J$. Le_J is the Lewis number of chemical species J which can be obtained from references. For example, $Le_{C_3H_8} = 1.74$, $Le_{O_2} = 1.11$, $Le_{H_2O} = 0.83$, $Le_{CO_2} = 1.39$ and $Le_{N_2} = 1$ (Smooke 1991; Giacomazzi, Picchia & Arcidiacono 2008). The parameter κ ($W\,(m^{-1}{\cdot}K^{-1})$) is the thermal conductivity modelled by the modified Eucken correction (Poling, Prausnitz & O'Connell 2001)

$$\kappa = \mu C_v \left(1.32 + \frac{1.77R}{C_v} \right), \tag{2.8}$$

where R is the gas constant ($J\,(kg^{-1}{\cdot}K^{-1})$), C_v is the heat capacity at the constant volume ($J\,(kg^{-1}{\cdot}K)^{-1}$) and D_J^T ($kg\,(m^{-1}{\cdot}s^{-1})$) is the thermal diffusion coefficient. Maragkos, Beji & Merci (2017) adopted the following formula in their version of FireFOAM:

$$D_J^T = -2.59 \times 10^{-7} \tilde{T}^{0.659} \left[\frac{M_J^{0.511} X_J}{\sum_J M_J^{0.511} X_J} - \tilde{Y}_J \right] \left[\frac{\sum_J M_J^{0.511} X_J}{\sum_J M_J^{0.489} X_J} \right], \tag{2.9}$$

where M_J is the molecular weight of chemical species J and X_J is the volume fraction of chemical species J.

The value of μ is estimated by Sutherland's law (OpenFOAM v2006 2020)

$$\mu = \frac{A_s \tilde{T}^{0.5}}{1 + T_s/\tilde{T}}, \tag{2.10}$$

where $A_s = 1.67212 \times 10^{-6}$ ($kg\,(m{\cdot}s{\cdot}K^{0.5})^{-1}$), and $T_s = 170.672$ (K).

2.2.2. *Turbulence model*

The Smagorinsky model is a widely used and successful sub-grid-scale model (Smagorinsky 1963), known as one of the most basic sub-grid-scale models for LES. However, the model has a parameter, the Smagorinsky constant (C_s), whose value depends on the characteristics of the flow. The dynamic Smagorinsky model is an improved version of the Smagorinsky model that allows C_s to be determined dynamically in both time and space (Germano *et al.* 1991 and Lilly 1992). In the Smagorinsky model, μ_{SGS} is computed by

$$\mu_{SGS} = \bar{\rho} \left(C_s \Delta_{filter} \right)^2 |\tilde{S}|, \tag{2.11}$$

$$\tilde{S}_{ij} = \frac{1}{2}\left(\frac{\partial \tilde{u}_i}{\partial x_j} + \frac{\partial \tilde{u}_j}{\partial x_i}\right), \, |\tilde{S}| = \sqrt{2\tilde{S}_{ij}\tilde{S}_{ij}}, \tag{2.12}$$

where Δ_{filter} is the filter width (m) and $\tilde{S}$ is the symmetrical component of the velocity gradient tensor (s^{-1}). The parameter C_s is estimated as

$$C_s^2 = \frac{1}{2}\frac{\langle L_{ij}M_{ij}\rangle}{\langle M_{kl}M_{kl}\rangle}, \tag{2.13}$$

$$L_{ij} = \left(\widehat{\tilde{u}_i\tilde{u}_j} - \hat{\tilde{u}}_i\hat{\tilde{u}}_j\right), \tag{2.14}$$

$$M_{kl} = \Delta_{filter}^2\left(\widehat{|\tilde{S}|\tilde{S}_{kl}} - 4|\hat{\tilde{S}}|\hat{\tilde{S}}_{kl}\right), \tag{2.15}$$

where $\langle \rangle$ is an area-weighted average, L_{ij} is called the Germano identity and $\widehat{}$ is the value of the test filter for the dynamic Smagorinsky model with the width of the test filter given as $\hat{\Delta}_{filter} = 2\Delta_{filter}$. The value of μ_{SGS} has been obtained up to this point. For the combustion model, it is necessary to estimate the sub-grid-scale turbulent kinetic energy (k_{SGS}, (m^2 s^{-2}))

$$k_{SGS} = C_I\Delta_{filter}^2|\tilde{S}|^2, \tag{2.16}$$

where C_I is the model constant for k_{SGS}

$$C_I = \frac{\langle KN\rangle}{\langle N^2\rangle}, \tag{2.17}$$

$$K = \frac{1}{2}\left(\widehat{\tilde{u}_i\tilde{u}_j} - \hat{\tilde{u}}_i\hat{\tilde{u}}_j\right), \tag{2.18}$$

$$N = \Delta_{filter}^2\left(4|\hat{\tilde{S}}|^2 - \widehat{|\tilde{S}|^2}\right). \tag{2.19}$$

In OpenFOAM v2006 2020, the dynamic Smagorinsky model is not included. Passalacqua (2021) introduced this model, and we previously integrated it into the in-house version of FireFOAM (Fukumoto *et al.* 2019).

For completeness, a direct comparison between the incompressible and compressible formulations of the dynamic Smagorinsky model is shown in figure 22 of Appendix A. As shown there, the density correction has a negligible effect on both the temperature rise and the velocity distribution; accordingly, the incompressible formulation of the model is adopted throughout this study.

2.2.3. *Combustion model*

Magnussen & Hjertager (1977) initially suggested the eddy dissipation model and later extended it to the eddy dissipation concept model (Magnussen 1981). The eddy dissipation concept models the average reaction rate by considering the process of dissipating energy from the large to small scale. However, since the variables in the model are from the Reynolds average Navier–Stokes simulation (RANS), a problem arises with the direct replacement of variables when applying it to the LES. For example, the RANS-based epsilon and sub-grid-scale epsilon are different. Chen *et al.* (2014) re-constructed the eddy dissipation turbulence energy cascade model proposed by Ertesvåg & Magnussen (2000) to match the scale of the LES model. Their model has been applied to a variety of

combustion scenarios by LES: pool fires (Chen *et al.* 2014; Wang, Wen & Chen 2014a), jet flames (Wang *et al.* 2014b; Fukumoto *et al.* 2019), flame spread (Fukumoto, Wang & Wen 2022) and buoyant diffusion flames (Chen *et al.* 2023b). This section presents the essential information for implementation.

The energy dissipation concept uses the length scale on the last structure level, L^* (m), and the velocity scale on the last structure level u^* (m s^{-1}). The reaction takes place in these scales. Chen *et al.* (2014) estimated those as

$$L^* = \frac{2}{3} \left(\frac{3C_{D2}^3}{C_{D1}^2} \right)^{1/4} \left(\frac{\nu^3}{\varepsilon_{tot}} \right)^{1/4}, \tag{2.20}$$

$$u^* = \left(\frac{C_{D2}}{3C_{D1}^2} \right)^{1/4} (\nu \varepsilon_{tot})^{1/4}, \tag{2.21}$$

where ε_{tot} is the total epsilon and ν is the kinematic viscosity. From these derivations, Chen *et al.* (2014) assumed that the smallest scale ($=$ last structure level) is the Kolmogorov length, and they derived $C_{D1} = 0.5$ and $C_{D2} = 0.75$. Chen *et al.* (2014) also modelled the total dissipation energy, ε_{tot}, (m^2 s^{-3}) based on the energy cascade concept

$$\varepsilon_{tot} = \sqrt{\frac{2}{3}} C_{D1} \frac{k_{SGS}^{3/2}}{\Delta_{filter}} + \frac{2}{9} C_{D2} \nu \frac{k_{SGS}}{\Delta_{filter}^2}, \tag{2.22}$$

where Δ_{filter} is the filter width (m) and k_{SGS} is the sub-grid-scale turbulent kinetic energy (m^2 s^{-2}). Thus far, these equations are the formulation of the variables that link the eddy dissipation concept to the LES. For the detailed derivation of this model, readers should refer to Chen *et al.* (2014). It is now possible to determine the reaction rate using the eddy dissipation concept model. The reaction rate of chemical species J is given by

$$\bar{\omega}_J = \left(\nu_J'' - \nu_J' \right) \frac{M_J}{M_{fu}} \bar{\omega}_{fu}, \tag{2.23}$$

$$\bar{\omega}_{fu} = \bar{\rho} \dot{m}^* \frac{\gamma \chi}{1 - \gamma \chi} min \left(\tilde{Y}_{fu}, \frac{\tilde{Y}_{O_2}}{s} \right), \tag{2.24}$$

where $\bar{\omega}_J$ is the reaction rate of chemical species J, ν_J' and ν_J'' are the molar stoichiometric coefficients on the left- and right-hand sides of the global reaction equation, $\dot{m}^*$ is the mass transfer rate between fine structures and surrounding fluids (s^{-1}), γ is the mass fraction of fine structures, χ is the reacting fraction of fine structures, s is the stoichiometric O$_2$-to-fuel mass ratio and subscripts fu and O$_2$ are fuel and oxygen, respectively,

$$\gamma = \left(\frac{L^*}{L'} \right)^\alpha, \tag{2.25}$$

$$L' = \left(\frac{\dot{Q}}{\rho_\infty C_{p,\infty} T_\infty \sqrt{g}} \right)^{2/5}, \tag{2.26}$$

$$\chi = \begin{cases} \dfrac{\tilde{Z}}{Z_{st}}, & 0 \leqslant \tilde{Z} < Z_{st}, \\[2mm] \dfrac{1 - \tilde{Z}}{1 - Z_{st}}, & Z_{st} \leqslant \tilde{Z} \leqslant 1, \end{cases} \tag{2.27}$$

where L' is the integral scale (m), $\tilde{Z}$ is the mixture fraction, Z_{st} is the mixture fraction at the stoichiometric state, $\alpha = 0.2$ and $\dot{Q}$ is the heat release rate (W).

The mass transfer rate between fine structure and surrounding fluids is modelled as (Ertesvåg & Magnussen 2000)

$$\dot{m}^* = \frac{2u^*}{L^*} = \left(\frac{3}{C_{D2}}\right)^{1/2} \left(\frac{\varepsilon_{tot}}{\nu}\right)^{1/2}. \tag{2.28}$$

3. Results

3.1. *Experiment*

3.1.1. *Two modes of flame behaviour in the spanwise direction*

For two proximal tandem filaments, it was found that they obviously undulate in the spanwise direction (Zhu 2009). It is instructive to compare the behaviour of tandem filament motions with analogous views of tandem diffusion flames. Time variation of representative frames for two tandem fires separated by varying distances S in the spanwise direction under relatively strong cross-airflow is exhibited in figure 2. From the overhead view, it is of interest to observe that both flames flap, i.e. flame tip waves back and forth in the spanwise direction, in particular, the downstream following flame takes on greater lateral amplitude in figure 2(*a*) that is identical to flexible objects (Zhu 2009).

From the top and left of figure 2(*a*), the arc shape of the DDF directly reflects the instantaneous wake vortex to a great extent, which indicates that this oscillation phenomenon is closely associated with the invisible flow structures. Due to the presence of soot, the luminous flame itself is a natural flow-field tracer to some extent. Based on experimental observation, two modes were distinguished through the flame phenomena. Firstly, the flapping behaviour of flames in the spanwise direction is defined as mode I–'oscillating mode'. In addition to the oscillating mode, symmetrical or asymmetrical bifurcation of the flame to the left and right sides is in the DDF, as depicted in figure 2(*b*). This bifurcation phenomenon is barely noticeable for the UDF. In the meantime, it is also observed that the maximum width of this wing-like structure in the spanwise direction seems to increase as the spacing enlarges. In this case, the second mode is defined as mode II–' bifurcating mode'. Through the playback of the recorded video, one can observe that these two aforementioned modes alternately appear at random. Note that these phenomena only exist in cross-wind-dominated cases ($u_c \geqslant 1.2 \text{ m s}^{-1}$).

The formation of these two modes indicates that the oscillation or bifurcation of the DDF strongly depends on the flow structure downwind of the UDF. Shinohara & Kudo (2004) identified several types of vortices downstream of a diffusion flame by the flow visualisation technique. One of them is wake vortices, which consists of periodical vortices of alternating signs (i.e. including cyclonic and anticyclonic rotation), similar to the Kármán vortex street. However, this kind of wake vortex is not as well ordered as the Kármán vortex street owing to the coupling actions of the buoyancy and drag forces (Zhu 2009). For the oscillating mode, downstream flame synchronous flaps form under the action of wake vortices shedding from the UDF at the height above the burner surface. Thus, one could observe that flames with arcs occasionally occur. The flapping mechanism is explained by simulation in § 3.2.3.
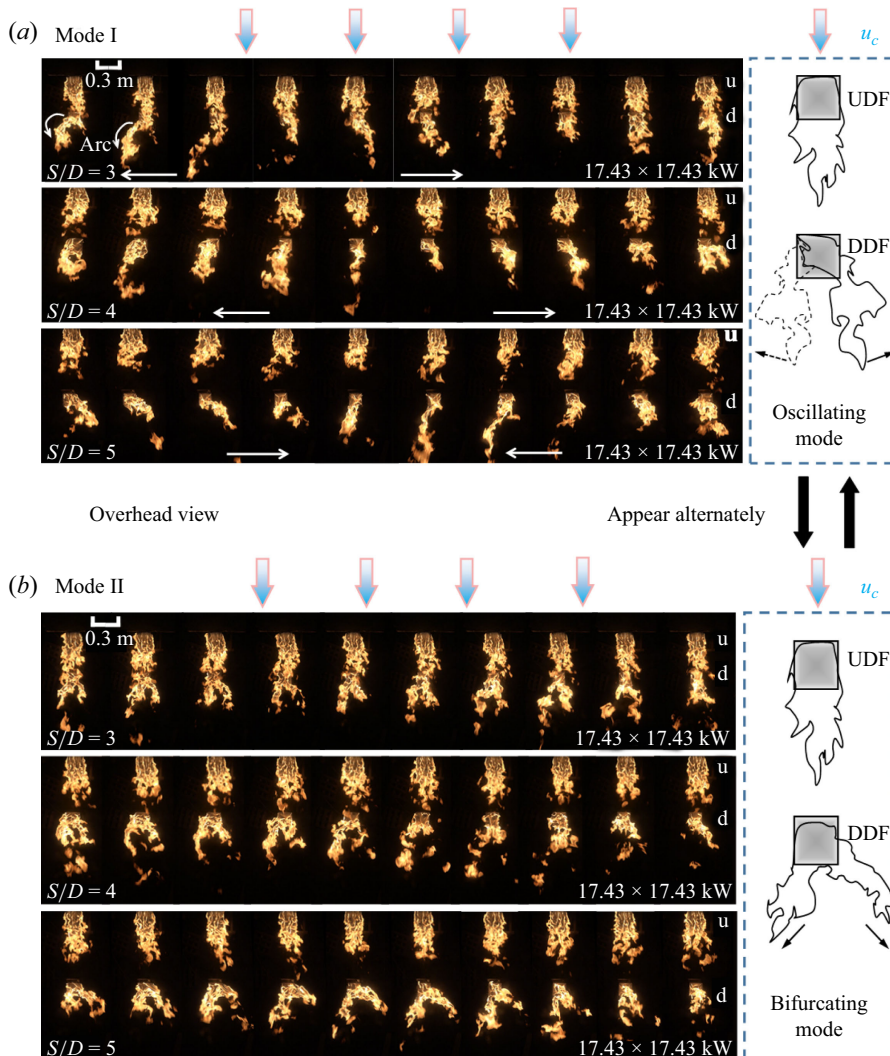
Figure 2. Selected frames at the interval of 0.04 s revealing the two motion modes for DDF under relatively strong cross-wind ($u_c = 2$ m s^{-1}) at different spacings for non-merging cases: (*a*) mode I: oscillating mode; (*b*) mode II: bifurcating mode. See also Movie 1 about the experimental overhead video image at $u_c = 2$ m s^{-1}, $S/D = 3$ and $\dot{Q}_u = 17.43$ kW and $\dot{Q}_d = 17.43$ kW.

To further characterise the flame motion behaviour in the spanwise direction, it is of interest to capture the instantaneous flame edge position versus the elapsed time. The upper/lower edge of the flame represents the widest location along the spanwise direction where the flame could reach. In order to objectively track the upper/lower flame edge, each frame is loaded into a MATLAB script and converted to a bitonal picture. Then, the upper/lower edges of UDF and DDF can be extracted via MATLAB, which is defined as the distance between the burner centreline and the upper/ lower flame edge. Figure 3 shows an instantaneous measure of the upper/lower flame edge normalised by D with the increasing u_c at a given separation distance, where both fires have the same heat release rate of 17.43 kW. In figure 3, firstly, we define up as positive and down as negative, employing the burner centre as the coordinate origin. Then, the coordinates of
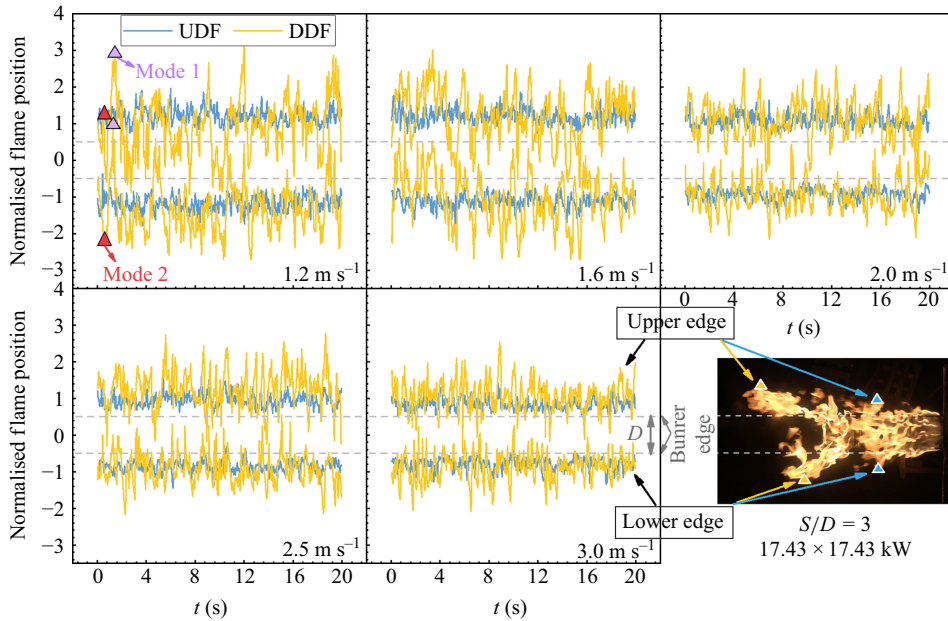
Figure 3. Normalised flame position of the upper edge and lower edge as a function of time under varied cross-wind velocities for the UDF and DDF ($S/D = 3$, $\dot{Q}_u = 17.43$ kW and $\dot{Q}_d = 17.43$ kW).

the upper/lower edges of the UDF and DDF can be obtained. Finally, instantaneous flame upper/lower edges with the elapsed time are normalised by burner size D. Blue and orange solid lines represent the UDF and DDF edges' positions, respectively. Grey dash lines represent the edge of the burner, and '0' corresponds to the burner centre. The oscillating and bifurcating modes are defined as follows:

$$x_{norm,lowedge} - \bar{x}_{norm,lowedge} < 0 \wedge x_{norm,upedge} - \bar{x}_{norm,upedge} > 0 \qquad (3.1)$$
$$\text{if satisfied:} \quad \text{Bifurcating mode}$$
$$\text{else:} \quad \text{Oscillating mode},$$

where $x_{norm,upedge}$, $\bar{x}_{norm,upedge}$, $x_{norm,lowedge}$ and $\bar{x}_{norm,lowedge}$ are the normalised upper flame edge position, the time-averaged normalised upper flame edge position, the normalised lower flame edge position and the time-averaged normalised lower flame edge position. When the position of the flame edge on both sides is greater than the average of each side, the bifurcating mode is assumed. Otherwise, the oscillating mode is assumed. The absolute value of either or both should be greater than or equal to that of the UDF in light of the asymmetry in bifurcation. This definition can be a quantitative standard to distinguish these two modes.

Typical oscillating and bifurcating mode examples have been marked in figure 3. Some notable observations can be made that: (i) the DDF behaviour is much more disordered than that of the UDF, while the amplitude of upper and lower edges of the UDF is narrower than that of the DDF; (ii) the amplitude of upper and lower edges for either the UDF or DDF have a declining trend as u_c increases, the amplitude of the edge of the DDF at 1.2 m s^{-1} is almost twice that of the DDF with $u_c = 3.0$ m s^{-1}. The occurrence of the oscillating and bifurcating modes seems irregular. This trend would be due to the flame self-sustained oscillatory frequency, cross-flow turbulence intensity and the fire size and strength. Figure 4 shows the power spectrum vs frequency analysed by the fast Fourier
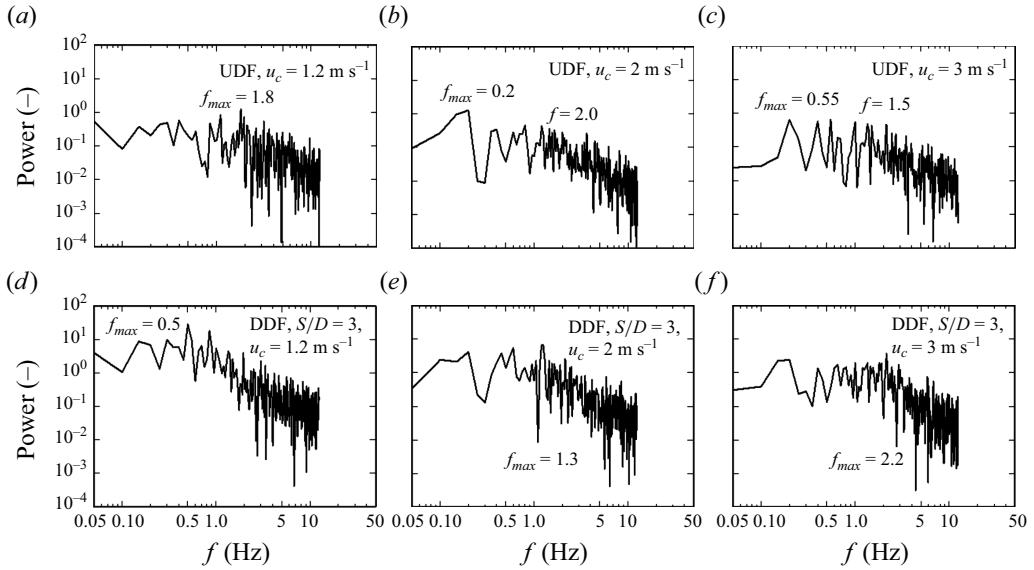
Figure 4. Power $(-)$ vs frequency f (Hz) by the fast Fourier transform of the flame position data in figure 3, where f is the frequency and f_{max} is the peak frequency. The results are shown for following cases: (*a*) UDF, $u_c = 1.2\ \mathrm{m\,s^{-1}}$, (*b*) UDF, $u_c = 2.0\ \mathrm{m\,s^{-1}}$, (*c*) UDF, $u_c = 3.0\ \mathrm{m\,s^{-1}}$, (*d*) DDF, $S/D = 3$, $u_c = 1.2\ \mathrm{m\,s^{-1}}$, (*e*) DDF, $S/D = 3$, $u_c = 2.0\ \mathrm{m\,s^{-1}}$ and (*f*) DDF, $S/D = 3$, $u_c = 3.0\ \mathrm{m\,s^{-1}}$. Here, $\dot{Q}_u = 17.43$ kW and $\dot{Q}_d = 17.43$ kW. Note that, if the frequency at which the curve drops is not equal to f_{max}, its frequency is also indicated (see (*b*) and (*c*)).

transform (FFT) of the flame position data in figure 3, where f is the frequency, and f_{max} is the peak frequency in figure 3. The peak power of the UDFs appears at approximately 0.2–1.8 Hz, and that of the DDFs shows 0.5–2.2 Hz, which is approximately similar to a puffing frequency of buoyancy flames and pool fires (Cetegen & Ahmed 1993; Maragkos & Merci 2020). The main spanwise flapping occurs at these frequencies. The power spectrum decreases steadily, which indicates that the high-frequency component has less power than the low-frequency component. Due to the influence of the UDF, the power is higher for the DDF than for the UDF. For the slower u_c, the power is also higher because the DDF is affected by the UDF, resulting in a larger oscillation width. A faster u_c results in less power because the oscillation width is reduced. Instead, in the DDF, f_{max} increases gradually as u_c increases, indicating that the flapping speed becomes fast. As u_c increases, the low-frequency component increases, resulting in a wave with a mixture of low- and high-frequency components. In other words, as u_c increases, the flapping becomes faster, the flame width decreases and flapping with various periods gets mixed together.

Furthermore, the sheltering effect of the UDF reduces the tilt angles of the DDF, and the tilt angles become smaller at a given cross-wind with the increasing burner distance for non-merged cases. The ratio of the flame tilt angle of the DDF to that of the UDF for non-merged cases was a function of a modified Froude number, $u_c^2/(gS)$. Note that this work focuses on the flapping behaviour under cross-wind ranging from 1.2 to 3.0 m s^{-1}, in which the thermal buoyancy caused by diffusion flames was overwhelmed by the inertial force of the cross-wind. The increasing rate of tilting angles for both the UDF and DDF gradually becomes slower with the further increase in cross-wind speed between 1.2 and 3.0 m s^{-1}. Given these conditions, tilting behaviour is not considered a primary factor in this study.
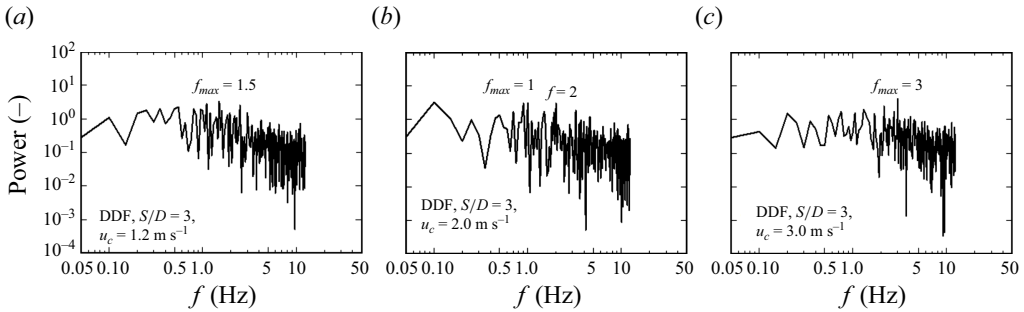
Figure 5. Power $(-)$ vs frequency f (Hz) by the FFT. The original data are the difference in the normalised flame position of the upper and lower edges of the DDF in figure 3. The bifurcating mode is set to 1, and the oscillating mode is set to 0 to create a square wave. The results are shown for following cases: (*a*) $u_c = 1.2$ m s^{-1}, (*b*) $u_c = 2.0$ m s^{-1}, (*c*) $u_c = 3.0$ m s^{-1} with $\dot{Q}_u = 17.43$ kW, $\dot{Q}_d = 17.43$ kW and $S/D = 3$. Note that, if the frequency at which the curve drops is not equal to f_{max}, its frequency is also indicated (see (*b*)).

The additional FFT data are shown in figure 5. The original data are the difference in the normalised flame position of the upper and lower edges of the DDF in the bifurcating mode. The original data were created based on the bifurcating mode $= 1$, and the oscillating mode $= 0$, indicating a square wave. By treating mode switching as if it were a signal switch, we attempted to identify its frequency. The parameter f_{max} is the fundamental frequency of the square wave around which mode switching is considered to occur. As shown in figure 5(*a*), (*b*) and (*c*), when u_c is fast, waves with higher energy tend to appear at higher frequencies. This trend may be due to the faster cross-wind velocity, leading to the flame oscillating more rapidly and more frequently switching modes. This is reflected in the increasing f_{max} from 1.5 Hz at $f_{max} = 1.2$ m s^{-1} (figure 5*a*) to 3 Hz at $f_{max} = 3.0$ m s^{-1} (figure 5*c*). Although there is such a tendency, several waves with different frequencies and powers appear, as shown in figure 5. Different frequencies appear in the spectra (with peaks at various frequencies), indicating that the mode switching is complex or non-periodic. For example, Xia & Zhang (2018) proposed a theory for the flickering phenomenon of small buoyant diffusion flames. However, this flame is more complex, as the UDF and DDF oscillate simultaneously on both the left and right sides. In other words, four waves oscillate independently. Thus, reproducing such a phenomenon using CFD is more reasonable than formulating it theoretically (see § 3.2).

3.1.2. *Maximum flame width magnitude in the spanwise direction*

The previous section exhibited an instantaneous phenomenon as a function of time. Since fire plume flow is usually turbulent, flame shape parameters such as horizontal flame extent and flame height are time-dependent and unsteady. As a result, time-averaged flame shape parameters are taken based on 50 % intermittency for analysis in some works (Zukoski, Cetegen & Kubota 1985; White *et al.* 2015; Maynard & Butta 2017; Sun *et al.* 2021). However, the objective of this work is to investigate the flapping behaviour of a pair of tandem diffusion flames under cross-wind, which focuses on the furthest distance the fires can reach in the spanwise direction because the neighbouring combustibles may be ignited due to flame contact. The maximum flame widths (W) in the spanwise direction have been identified, which aids in assessing the most dangerous fire scenarios, a factor often overlooked in previous research. Meanwhile, the maximum flame height corresponding to the 0.05 flame intermittency has also been addressed and analysed in fire research (Zukoski *et al.* 1985; Lee, Delichatsios & Silcock 2007; Zhou & Wu 2007; Shintani *et al.* 2014; Ji, Ge & Qiu 2021). Figure 6 shows the time-averaged maximum flame width (W) to
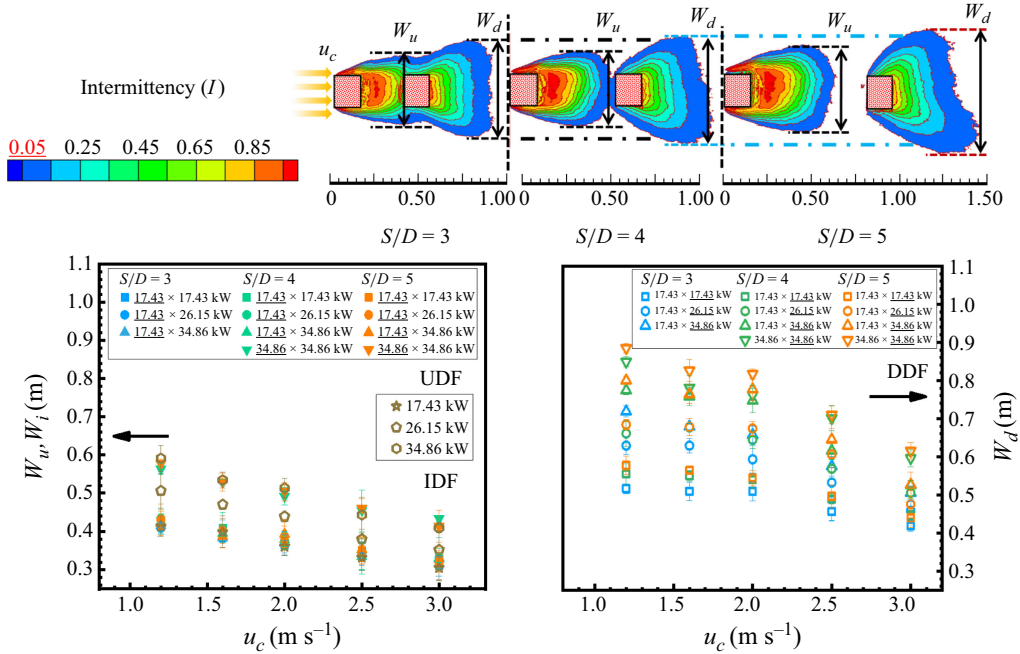
Figure 6. Intermittency of the presence of flame using recorded images (top) and measured maximum flame width against cross-wind speed (u_c) under various spacings (S) for non-merging cases (lower).

quantitatively describe this phenomenon. This width is defined as the maximum distance in the spanwise direction based on the lowest intermittency level ($I = 0.05$). Figure 6 compares the variation of measured W against cross-wind for the IDF (W_i), UDF (W_u) and DDF (W_d). It is observed that the maximum W_u for varying a separation distance (S) is nearly the same as W_i at a given heat release rate, which also becomes narrower as u_c increases. A small difference in W between the UDF and IDF implies that the DDF in cross-wind has a negligible effect on the UDF. The presence of the flame motion of the DDF indicates that the UDF has a strong influence on the DDF flapping movement.

It is also found that all the maximum widths of the IDF, UDF and DDF grow with the increasing $\dot{Q}$ due to the expansion of flame volume. Moreover, W_d is broader when raising $\dot{Q}_u$. Compared with the maximum W of the IDF and UDF, that of the DDF is found to be markedly larger. Meanwhile, it enlarges with the increasing S, which is consistent with the visual observations in figure 2. An intuitive physical interpretation is provided as follows. Since the flame is a natural indicator of the flow pattern, the flames are passive and follow the motion of surrounding fluid owing to fluid viscosity. The DDF is entirely immersed in the wake of the UDF. The motion of wind-blown UDF produces a disturbed vortex-embedded wake, which is helpful for the flapping behaviour of the DDF. As the two tandem flames are brought further apart, or the resistance of the UDF is strengthened (equal to higher $\dot{Q}$), the wake downstream should widen and disentangle (Ristroph & Zhang 2008). Hence, W_d is wider when separation distances are larger or the heat release rate of the UDF is larger. When there is a stronger cross-wind (>1.2 m s^{-1}), the sideways movement of both flames is limited (equal to lower W) by the force of the cross-wind. In other words, the interaction between these two fires is weaker, and W greatly depends on u_c (refer to figure 3).

A comparison of the maximum width of the UDF and DDF to that of the IDF is plotted in figure 7 as a function of $u_c^2/(gS)$ following Chen *et al.* (2021). In addition
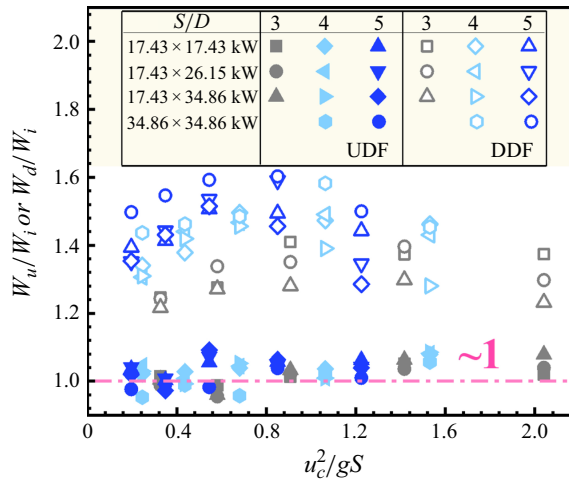
Figure 7. Ratio of the UDF or DDF maximum width to that of IDF as a function of modified $Fr = u_c^2/(gS)$.

to the phenomenon found above, one could also notice that W_d/W_i shows a non-monotonic trend. The first rising trend indicates that W_d decreases slower than W_i with increasing u_c. The following declining regime signifies that the wake structures downstream of the UDF become notably narrow under the increasing cross-wind effect. One can speculate that W_u/W_i tends to be almost unity when the cross-wind velocity is large enough before these flames blow out.

3.1.3. *Full-scale test vs laboratory test*

We experimented on tandem diffusion flames under cross-winds in §§ 3.1.1 and 3.1.2. In fire research, large-scale and full-scale tests are difficult to carry out because they require a well-controlled large-scale fire testing facility and are expensive. Therefore, the research often relies on laboratory-scale experiments, which provide valuable insights despite differences in scale. These data, such as the length scales of the flame geometry, are then subject to an analysis utilising classical scale modelling and dimensionless parameters to develop or generalise the resulting correlation. Similarities exist between the large-scale and laboratory-scale experiments, especially in flow behaviour. The scale modelling methods have been widely applied in fire research (Emori & Saito 1983; Quintier 1989) by preserving the most important terms. Emori & Saito (1983) suggested the scaling relations of velocity (u), time (t) and temperature (T) vs length scale (L): $u_{fs}/u_{ls} = (L_{fs}/L_{ls})^{0.5}$, $t_{fs}/t_{ls} = (L_{fs}/L_{ls})^{0.5}$ and $T_{fs}/T_{ls} = L_{fs}/L_{ls}$, where the subscripts fs and ls denote full scale and laboratory scale. In our work, the heat release rate (HRR) adapted in the experiments ranges from 17.43 to 34.86 kW, and the burner size is 15 cm. The dimensionless HRR (expressed as $\dot{Q}^* = \dot{Q}/[\rho_\infty C_{p,\infty} T_\infty g^{1/2} D^{5/2}]$) is approximately 1.8–3.6, where subscript ∞ denotes ambient with $T = 293.15$ K. During preliminary tests, it was observed that the flapping behaviour of diffusion flames occurs when the cross-wind velocity $u_c > 1.2\,\mathrm{m\,s^{-1}}$. To better understand the scaling effects, we consider experimental data from relatively larger-scale fire tests as a reference. According to the results of large-scale fully turbulent pool fire tests (Lei *et al.* 2022*b*), for a diesel pool fire with a side length of 7 m, the theoretical heat release rate can reach 100 MW, and the dimensionless HRR is around 0.7. The dimensionless HRR of large-scale pool fires is at the same magnitude as that
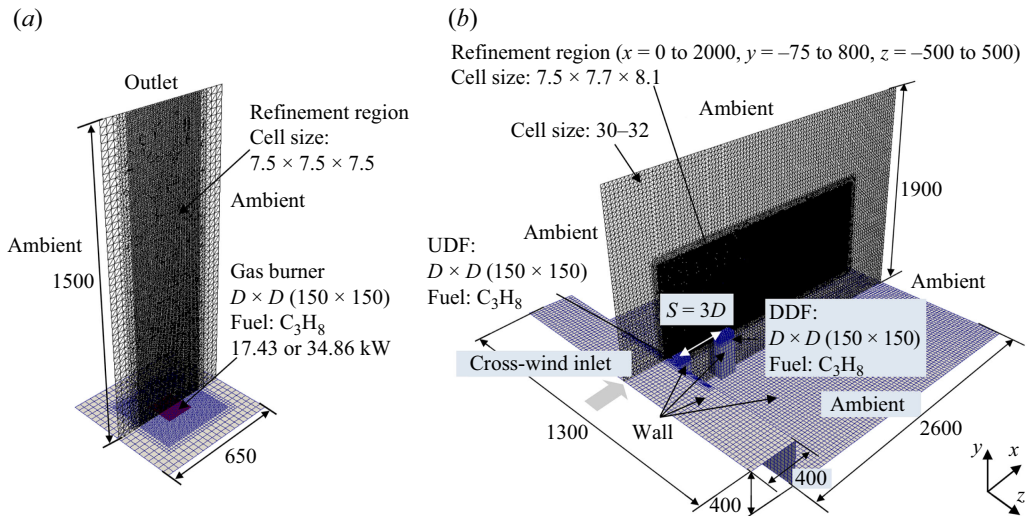
Figure 8. Computational domains for (*a*) a square burner and (*b*) tandem square burners with $S/D = 3$.

on the laboratory scale. Based on the scaling relation, the critical velocity at which the flame-flapping behaviour occurs should be approximately

$$u_{fs} = u_{ls} \left(\frac{L_{fs}}{L_{ls}} \right)^{1/2} = 1.2 \times \left(\frac{7}{0.15} \right)^{1/2} = 8.2 \, \text{m s}^{-1}. \quad (3.2)$$

In real fire situations, wind speeds of 10 m s^{-1} or higher are quite common, especially in areas prone to wildfires and during urban fire incidents. Large-scale fire experiments and field observations have documented wind conditions that exceed this threshold, which significantly impacts fire behaviour (Liu *et al.* 2021). For instance, extreme wildfire events have been documented with wind speeds that can range from 2 to 40 m s^{-1} (Finney & McAllister 2011), contributing to rapid fire spread and dynamic flame behaviour. Given these conditions, flame-flapping phenomena in the spanwise direction are expected to occur in large-scale fires where the length scales are of the order of 10 m, and the heat release rates range from 1 to 100 MW.

3.2. *Simulation*

Sections 3.1.1 and 3.1.2 used luminous flames as flow-field tracers. However, this method cannot observe variables in the flow field, such as temperature and velocity vectors. In this section, we visualise the flow using simulations to understand the two modes better.

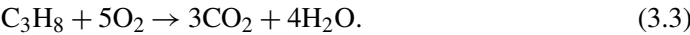### 3.2.1. *Computational conditions and domains*

Figure 8 shows the computational meshes and domains for (*a*) a square burner and (*b*) tandem square burners with $S/D = 3$. The computational mesh for the square burner was used for validation, while the mesh for the tandem square burners was constructed based on the experimental set-up. Figure 8(*b*) shows the domain for $S/D = 3$. The burner shape was square with 150×150 mm, and the burner spacings were $S/D = 3$, 4 and 5. The computational domains with $S/D = 4$ and 5 are shown in figure 23 of Appendix B.

Name	u	p_{rgh}[6]	
Gas burner	flowRateInletVelocity[1]	fixedFluxPressure	
Ambient	pressureInletOutletVelocity[2]	totalPressure[7]	
Outlet	inletOutlet[3]	fixedFluxPressure	
UDF/DDF	flowRateInletVelocity	fixedFluxPressure	
Cross-wind inlet	turbulentDFSEMInlet[4]	fixedFluxPressure[8]	
Wall	fixedValue[5]	fixedFluxPressure	

Name	Y_J	h (T condition)	ν_{SGS}
Gas burner	totalFlowRateAdvectiveDiffusive[9]	fixedValue[12]	zeroGradient
Ambient	inletOutlet[10]	inletOutlet[13]	zeroGradient
Outlet	inletOutlet[10]	inletOutlet[13]	zeroGradient
UDF/DDF	totalFlowRateAdvectiveDiffusive[9]	zeroGradient[14]	zeroGradient
Cross-wind inlet	fixedValue[11]	fixedValue[12]	zeroGradient
Wall	zeroGradient	zeroGradient	nutUSpalding WallFunction[15]

Table 1. Boundary conditions for a square burner and tandem square burners. Boundary condition names, such as inletOutlet, are defined in the documentation (OpenFOAM v2006 2020). The names are associated with those in figure 8.

[1]The Dirichlet condition based on a mass or volumetric flow rate.

[2]The Neumann condition with a zero gradient is applied. When backflow occurs u_i is specified based on the pressure.

[3]The Neumann condition with a zero gradient is applied. When backflow occurs, $u_i = 0$ is set.

[4]The synthesised-eddy based velocity inlet condition, which is the Dirichlet condition. See more details in the documentation (OpenFOAM v2006 2020)

[5]The no-slip condition.

[6]In FireFOAM, p is not solved. p_{rgh} is solved, instead.

[7] $p_{rgh} = p_{ref} - 0.5\rho|u|^2$, where p_{ref} is 101,325 Pa.

[8]The Neumann condition with a zero gradient for pressure.

[9]The convective/diffusive condition. The zero gradient condition and the Dirichlet condition are mixed based on the ratio of convection and diffusion. When convection is strong, $Y_{C_3H_8}$ (fuel mass fraction) $= 1$. See more details in the documentation (OpenFOAM v2006 2020) or the authors' previous study (Fukumoto *et al.* 2018).

[10]The Neumann condition with a zero gradient is applied. When backflow occurs, $Y_{O_2} = 0.233$ and $Y_{N_2} = 0.767$ are set.

[11] $Y_{O_2} = 0.233$ and $Y_{N_2} = 0.767$.

[12] $T = 293.15$ K.

[13]The Neumann condition with a zero gradient is applied. When backflow occurs, $T = 293.15$ K is set.

[14]The Neumann condition with a zero gradient is applied to the quartz-sand burner surface. The burner consists of a porous sand layer, where fuel exits through designated inlet regions (flowRateInletVelocity, see footnote 9). The remaining solid surface is treated as adiabatic to account for the insulating properties of the quartz sand.

[15] ν_{SGS} is the SGS kinematic viscosity, given by the Spalding wall function.

Table 1 summarises the boundary conditions, where the names used in figure 8 (e.g. gas burner) for the boundary conditions are consistent. The fuel was C_3H_8, and the irreversible one-step chemistry model was used

$$C_3H_8 + 5O_2 \rightarrow 3CO_2 + 4H_2O. \tag{3.3}$$

Cross-wind u_c was not set for (*a*) the square single burner cases and was set for (*b*) the tandem-square-burner cases. Table 2 lists the computational conditions for tandem

Case	1	2	3	4	5	6	7	8	9	10	11	12
S/D	3	3	3	3	3	3	3	3	3	3	3	3
u_c	1.2	2.0	3.0	1.2	2.0	3.0	1.2	2.0	3.0	1.2	2.0	3.0
$\dot{Q}_{u \ or \ i}$	17.43	17.43	17.43	34.86	34.86	34.86	17.43	17.43	17.43	17.43	17.43	17.43
$\dot{Q}_d$	0	0	0	0	0	0	17.43	17.43	17.43	34.86	34.86	34.86

Case	13	14	15	16	17	18	19	20	21	22	23	24
S/D	4	4	4	4	4	4	5	5	5	5	5	5
u_c	1.2	2.0	3.0	1.2	2.0	3.0	1.2	2.0	3.0	1.2	2.0	3.0
$\dot{Q}_u$	17.43	17.43	17.43	17.43	17.43	17.43	17.43	17.43	17.43	17.43	17.43	17.43
$\dot{Q}_d$	17.43	17.43	17.43	34.86	34.86	34.86	17.43	17.43	17.43	34.86	34.86	34.86

Table 2. Computational conditions for the tandem square burners.
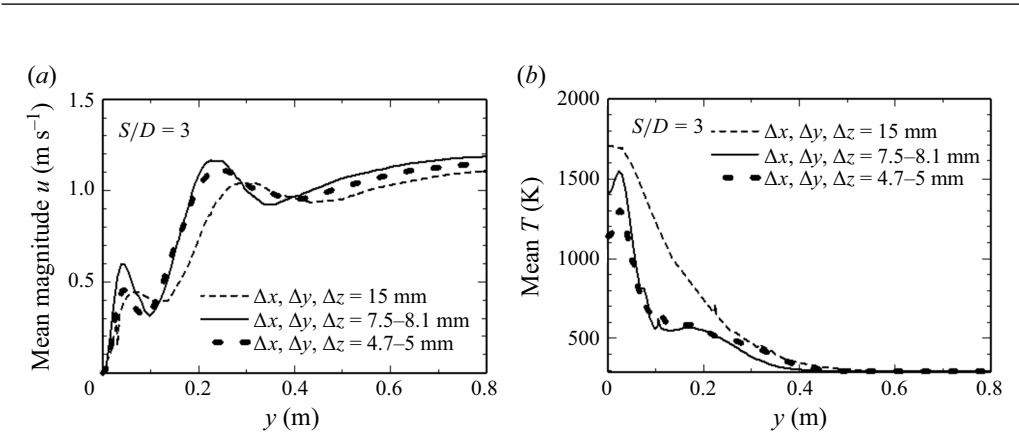
Figure 9. Mean magnitude u and T at different grid resolutions in the case of tandem square burners: $u_c = 1.2 \text{ m s}^{-1}$, $\dot{Q}_u = 17.43$ kW and $\dot{Q}_d = 34.86$ kW.

square burners. The value of S/D was varied from 3 to 5, the distance between burners. u_c was 1.2, 2.0 and 3.0 m s^{-1} and $\dot{Q}$ was set to 17.43 or 34.86 kW. At 293 K (the ambient condition) based on u_c, ρ_∞ and μ_∞, the Reynolds numbers are 11,400 ($u_c = 1.2$ m s^{-1}), 15,200 ($u_c = 1.6$ m s^{-1}), 19,000 ($u_c = 2.0$ m s^{-1}), 23,700 ($u_c = 2.5$ m s^{-1}) and 28,500 ($u_c = 3.0$ m s^{-1}). The Reynolds number is high enough to be considered turbulent with respect to the cross-wind.

3.2.2. *Grid dependency and validation*

Figure 9 shows the mean magnitude u and T at different grid resolutions in the refinement region in the case of tandem square burners. As shown in figure 9(*a*), the effect of the grid size on velocity is negligible. In contrast, as shown in figure 9(*b*), the predicted temperature is significantly affected when the grid widths are 15 and 7.5–8.1 mm. The velocities and temperatures at the finest mesh (4.7–5 mm) and medium mesh (7.5–8.1 mm) generally show good agreement. The number of cells on the coarsest mesh (15 mm) is approximately 920,000; on the medium mesh (7.5–8.1 mm), approximately 4,380,000; and on the finest mesh (4.7–5 mm), approximately 15,790,000. For the coarsest mesh, the effect of the cell size on the
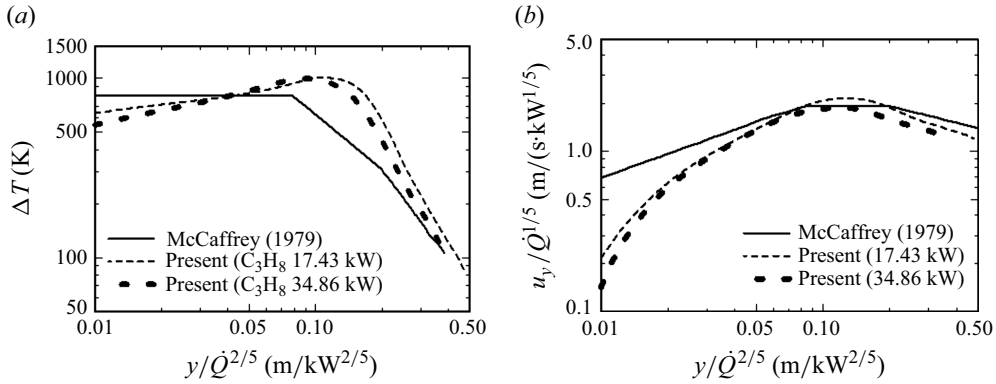
Figure 10. (*a*) Temperature rise (ΔT) and (*b*) normalised velocity ($u_y/\dot{Q}^{1/5}$) plotted against the normalised coordinate ($y/\dot{Q}^{2/5}$).
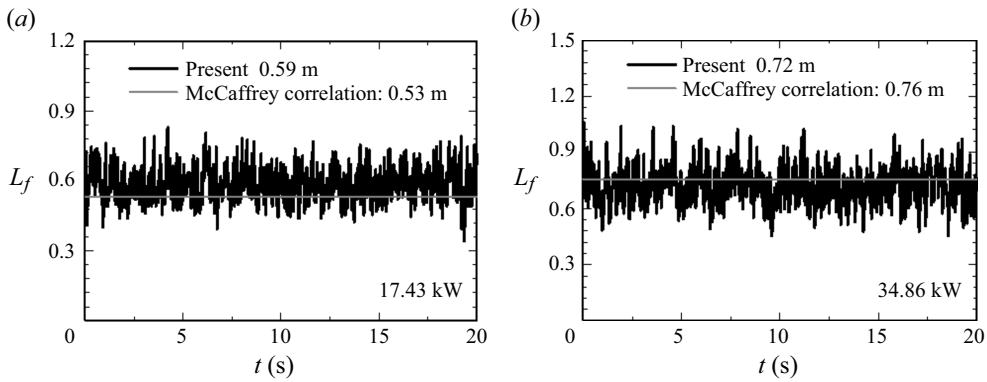

Figure 11. Flame heights (L_f) for square pool fires for heat release rates of (*a*) 17.43 and (*b*) 34.86 kW. The McCaffrey correlation (see (3.5)) is plotted for reference.

temperature cannot be ignored, and for the finest computational mesh, the computation time increases – therefore, an intermediate mesh of 7.5–8.1 mm was used in this study.

As an additional criterion, the plume resolution index (PRI) is evaluated

$$PRI = \frac{L'}{\Delta}, \tag{3.4}$$

where L' is obtained by (2.26), and Δ is the grid width (m). A value of $PRI = 5\text{--}15$ is an acceptable resolution according to the literature (Maragkos *et al.* 2017), and higher values correspond to a higher grid resolution. In this study, PRI is 25 for 17.43 kW and 33 for 34.86 kW. Thus, the grid resolution is sufficient.

Figure 10 shows (*a*) the temperature rise and (*b*) normalised velocity vs normalised coordinate. The correlation suggested by McCaffrey (1979) is plotted for reference. McCaffrey suggested the flame region for $y/\dot{Q}^{2/5} \leqslant 0.08$, intermittent region for $0.08 \leqslant y/\dot{Q}^{2/5} \leqslant 0.2$ and plume region for $0.2 \leqslant y/\dot{Q}^{2/5}$. The predictions match the trends in all three regions, but the temperature increase is approximately 200 K higher in the

intermittent region. The agreement between the predictions and McCaffrey's correlation is reasonable for the velocity prediction in the intermittency and plume regions.

Figure 11 shows flame heights L_f for heat release rates of (*a*) 17.43 kW and (*b*) 34.86 kW. The McCaffrey correlation (McCaffrey 1995; as cited in Heskestad 2016) is plotted for reference

$$L_f = -1.02D + 3.7\dot{Q}^{*2/5}D, \tag{3.5}$$

$$\dot{Q}^* = \frac{\dot{Q}}{\rho_\infty C_{p,\infty} T_\infty g^{1/2} D^{5/2}}. \tag{3.6}$$

The predicted flame height is estimated by the average of the highest coordinate values recorded during the simulations, for which the following equation is valid. This equation evaluates stoichiometric to fuel-rich conditions, the same as the previous study (Fukumoto *et al.* 2018)

$$\left[\frac{2Y_C}{M_C} + \frac{0.5Y_H}{M_H} - \frac{Y_O}{M_O} \right]_{fu} - \frac{Y_{O_2}}{M_O} \geqslant 0, \tag{3.7}$$

where subscripts C, H and O are respective elemental species. This criterion identifies all points where the local mixture fraction exceeds the stoichiometric value (3.7), and the flame height L_f is defined as the maximum coordinate satisfying this condition. Based on this definition, the errors for 17.43 and 34.86 kW are approximately 11 % and 5 %, respectively.

From figures 10–11, the accuracy of the calculation for single pool fires has now been verified. The next step is to verify the consistency between the measurements and predictions for tandem-square-burner scenarios. We consider the evaluation function closest to the experimentally defined intermittency shown in figure 6. The highest average T is assumed to be $I = 1$, since the probability of the existence of a flame is maximum. In contrast, the lowest average temperature (T_∞) is assumed to be $I = 0$ due to no flame. Based on this assumption, temperature at $I = 0.05$ is estimated by linear interpolation as

$$T_{I=005} = (1 - I_{005})T_\infty + I_{005}T_{max}, \tag{3.8}$$

where T_{max} and $T_{I=005}$ are the maximum temperature and the temperature with $I = 0.05$. Using the evaluation function for $T_{I=005}$, a three-dimensional isosurface was created to estimate the widths of the UDF and DDF.

The predicted flame width for tandem-square-burner cases compared with the experimental data is shown in figure 12. Figure 12(*a*) shows W_i, while all W_u are expected to be similar. Therefore, only $S/D = 3$ (*b*) and 5 (*c*) are plotted. The flame width trend shows that W_i and W_d decrease as u_c increases. Moreover, W_d is larger than W_i, and W_d increases as S/D increases, as discussed in § 3.1.2. For $u_c = 1.2$ and 2.0 m s^{-1} and $\dot{Q}_d = 34.86$ kW in figure 12(*h*), (*i*), there is a difference from the experimental data, especially where the flame width is measured to be large. Finally, the sensitivity of the predicted flame width to the burner height from the ground is shown in figure 24 of Appendix C, showing that variations in the burner height H (0.4 and 0.8 m) have only a marginal effect on the flame width under the present cross-flow conditions.

3.2.3. *Flapping mechanisms*

Equation (3.8) was used to determine how to estimate the flame width, which is close to the experimental intermittency. However, Yang & Blasiak (2005) proposed an alternative
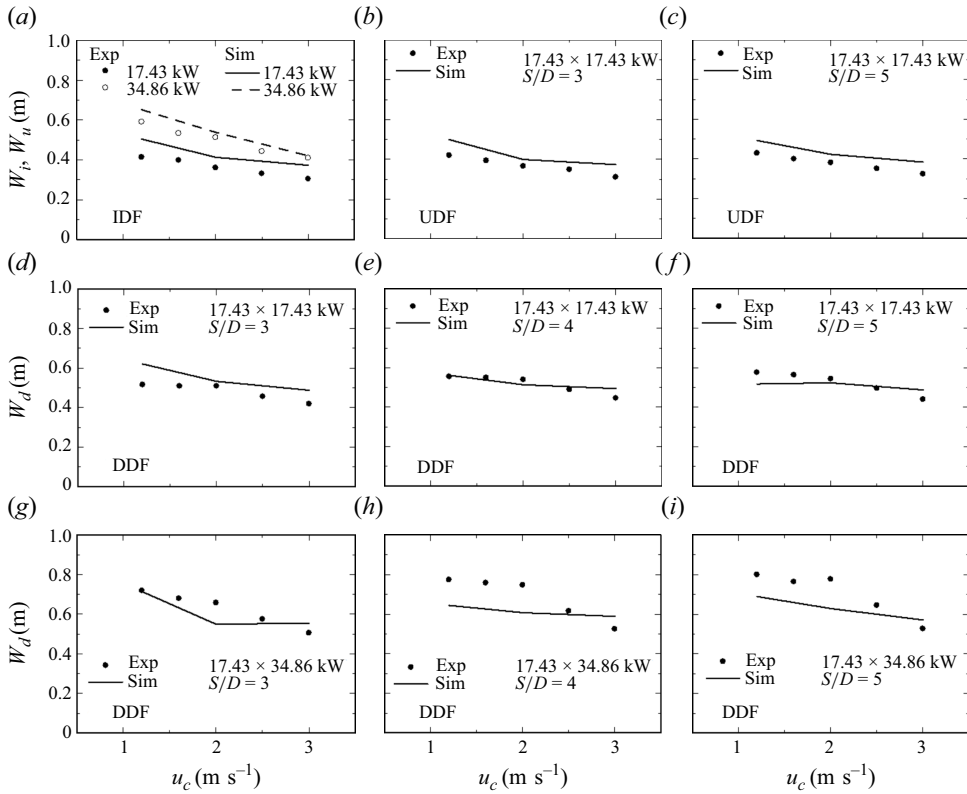
Figure 12. Predicted flame width for tandem-square-burner cases validated with the experimental flame width in figure 3.

flame-volume criterion as follows:

$$V_{fl} = \frac{1}{1 + s\tilde{Y}_{fu}/\tilde{Y}_{O_2}} \quad 0 \leqslant V_{fl} \leqslant 0.99, \tag{3.9}$$

where V_{fl} is the criterion for flame volume. This definition is particularly well suited for reproducing the visual appearance of flames on computers, such as those shown in figure 2.

Figure 13 shows the selected flames at an interval of 0.08 s for $S/D = 3$ and $u_c = 2.0 \text{ m s}^{-1}$ based on (3.9). As observed in the experiment, the simulation also confirms two modes, the oscillating and bifurcating modes. The time interval is 0.08 s, and changes in the flame tip can be observed in figure 13(*a*), (*b*). As described in § 2.2, the simulation uses the continuity, momentum, mass fraction, sensible enthalpy equations and general methods, such as a combustion model and a turbulence model, to obtain the solution and does not use a particular physical model for this problem. In other words, the flapping phenomenon is caused by a combination of fluid motion, concentration change, temperature change, turbulence and combustion. Furthermore, flames in the oscillating and bifurcating modes for $S/D = 4$ and $S/D = 5$ are shown in figure 14. Both simulations reproduce the two modes. In both modes, the flame widths at both ends increase with increasing S/D. In the oscillating mode, the flame width increases when the flame is biased in either direction, as shown in figure 14(*a*). In contrast, in figure 14(*c*), the flame moves to the centre, narrowing the flame width. In figure 14(*a*), (*c*), there are velocity
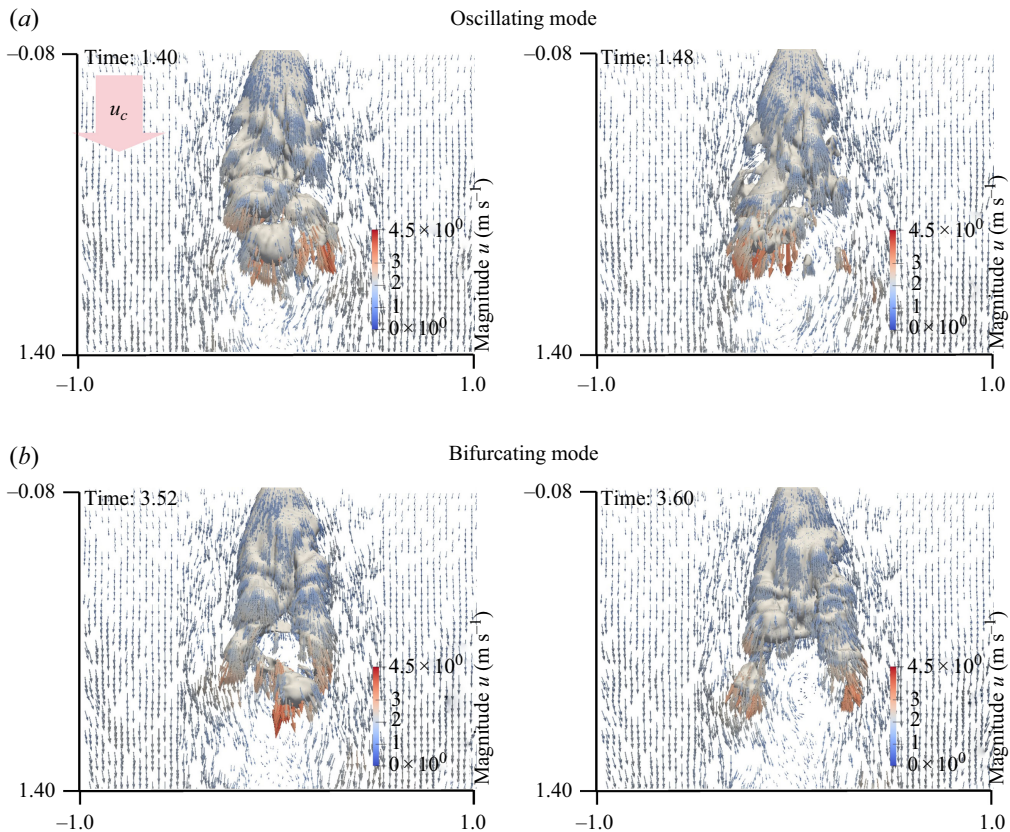
Figure 13. Selected flames at an interval of 0.08 s for $S/D = 3$, $u_c = 2.0$ m s^{-1}, $\dot{Q}_u = 17.43$ kW and $\dot{Q}_d = 17.43$ kW. See also Movie 2 for the computational video of flame volume and velocity vectors corresponding to $S/D = 3$, $u_c = 2.0$ m s^{-1}, $\dot{Q}_u = 17.43$ kW and $\dot{Q}_d = 17.43$ kW.

vectors in the opposite direction to the arc shape in the oscillating modes. This behaviour is explained by the wake vortices shed from the UDF. These vortices induce alternating flow patterns, causing the flame tips to oscillate. The flapping mechanisms will be described later (see figure 17). In the bifurcating mode, since the flame is open on both sides, the flame width is broader, as shown in figure 14(*b*), (*d*). From the fire safety point of view, the bifurcating mode is less desirable than the oscillating mode because the flame moves more in the spanwise direction.

Thus far, the oscillating mode and bifurcating mode were confirmed by the experiments and simulations. Next, the mechanisms of these modes are discussed. The overall flow in this system is shown in figure 15. The streams in this system exhibit strong three-dimensionality rather than a two-dimensional aspect, like the flow around the cylinder. This diagram explains how air is supplied by the environment under the cross-wind condition. There are four main streams. Stream (1) is a cross-wind along the burners. Stream (2) is a cross-wind away from the burner (approximately 0.65 m in the simulations). Streams (3) and (4) are entrainment air from the surroundings due to the UDF and DDF. Stream (3) is close to the UDF, and stream (4) is positioned on the outer side of the wake of both the UDF and DDF. Note that the computational domain in figure 15 is half. Stream (1) is considered to be the main flow component. Stream (2) lifts the flame at the location of stream (2)'. It is interesting that the fire is lifted by the cross-wind away from the fire
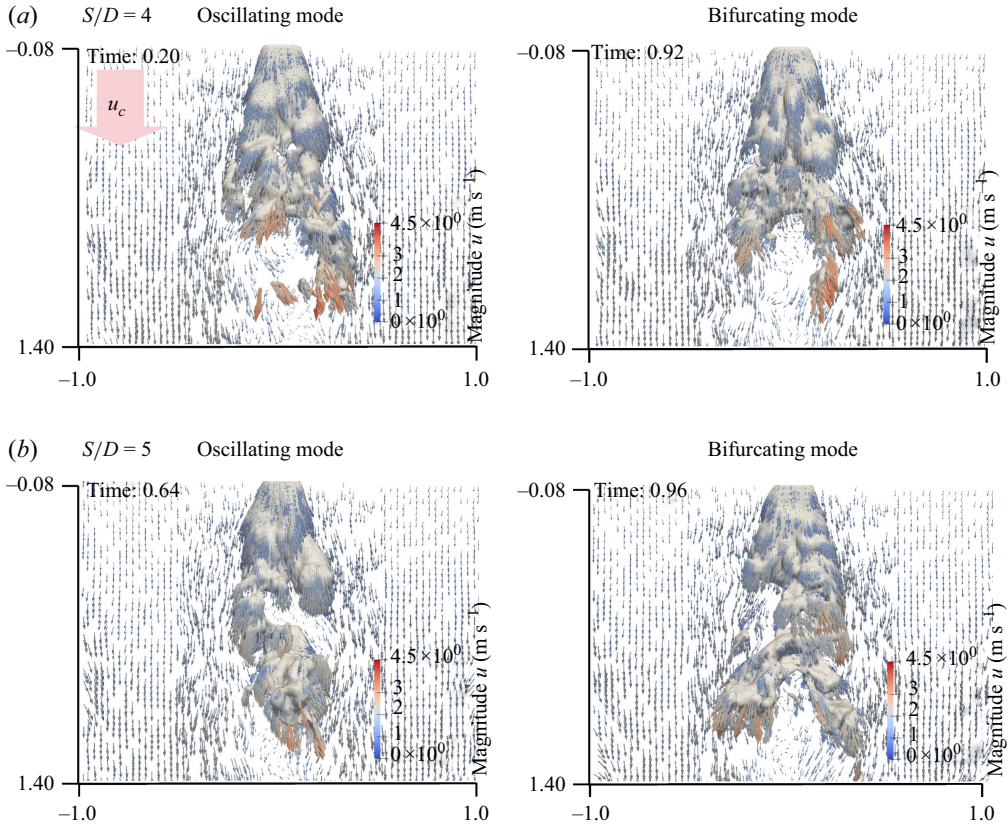
1014 A10-22

Figure 14. Selected flames for $u_c = 2.0$ m s^{-1}, $\dot{Q}_u = 17.43$ kW and $\dot{Q}_d = 17.43$ kW. Respective flames are (*a*) the oscillating mode for $S/D = 4$, (*b*) bifurcating mode for $S/D = 4$, (*c*) oscillating mode for $S/D = 5$ and (*d*) bifurcating mode for $S/D = 5$.
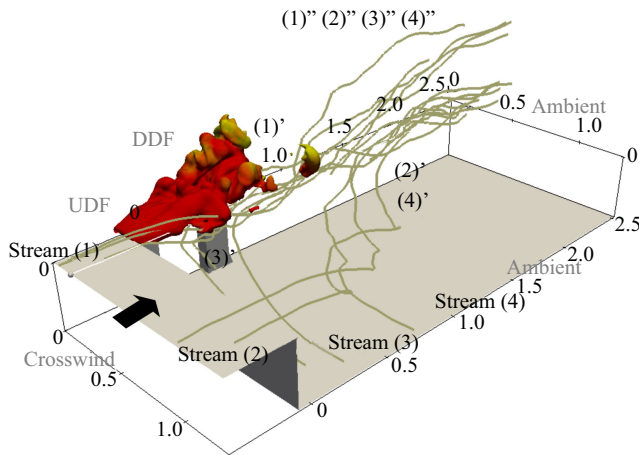

Figure 15. Streamlines for $S/D = 3$, $u_c = 2.0$ m s^{-1}, $\dot{Q}_u = 17.34$ kW and $\dot{Q}_d = 17.34$ kW. Stream (1) is a cross-wind near the burner. Stream (2) is a cross-wind slightly away from the burner. Streams (3) and (4) are entrainment air from the surroundings. Stream (3) is close to the UDF, and stream (4) is on the side of the wake of the UDF and DDF. Note that the gas flows move in the order of (No.), (No.)' and (No.)''. Only half of the computational domain is shown.
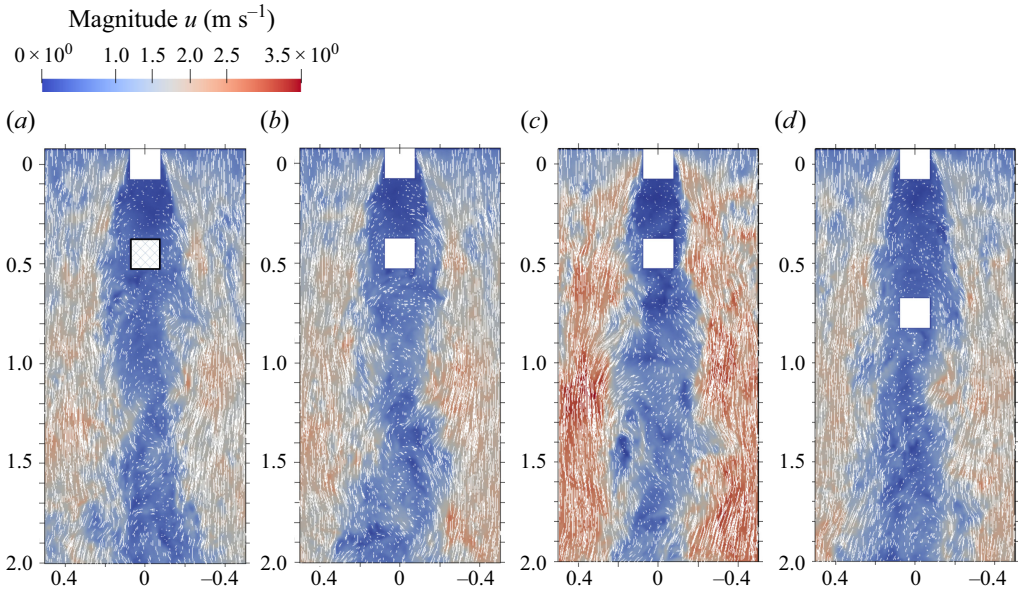
Figure 16. Velocity vectors for (*a*) IDF, $\dot{Q}_i = 17.43$ kW, (*b*) $S/D = 3$, $\dot{Q}_u = 17.43$ kW, $\dot{Q}_d = 17.43$ kW, (*c*) $S/D = 3$, $\dot{Q}_u = 17.43$ kW, $\dot{Q}_d = 34.86$ kW and (*d*) $S/D = 5$, $\dot{Q}_u = 17.43$ kW, $\dot{Q}_d = 17.43$ kW. The cross-wind velocity is $u_c = 2.0$ m s^{-1} on the $y = 0$ m surface.

source (stream (2)), even though the momentum direction is different. Stream (3) lifts the UDF wake and some of the DDF wake (stream (3)'). Stream (4) lifts the DDF wake (stream (4)'). Stream (4) merges with stream (2) beneath the DDF (see (2)'(4)'). The air is entrained toward the nearest fire source. In the end, streams (1)–(4) merge to form stream (1)"(2)"(3)"(4)". All the streams rise vertically because of the buoyancy caused by the fires.

Figure 16 shows the velocity vectors for the following cases: (*a*) the IDF with $\dot{Q}_i = 17.43$ kW, (*b*) tandem burners with $S/D = 3$, where $\dot{Q}_u = 17.43$ kW, $\dot{Q}_d = 17.43$ kW, (*c*) $S/D = 3$ with $\dot{Q}_u = 17.43$ kW, $\dot{Q}_d = 34.86$ kW and (*d*) $S/D = 5$ with $\dot{Q}_u = 17.43$ kW, $\dot{Q}_d = 17.43$ kW. For all the cases, the cross-wind velocity is $u_c = 2.0$ m s^{-1}. Additionally, (*b*) is in the bifurcating mode, (*c*) is in the oscillating mode and (*d*) is in the bifurcating mode. It is not easy to distinguish them by the velocity distribution, and flame volume is a better way to make these determinations (see figures 13 and 14). The red areas show a strong cross-wind effect, and the blue areas show the flame-caused velocity defect. The left and right flows do not intersect; the flapping generated on the left side of the UDF affects the flapping generated on the left side of the DDF. Likewise, flapping generated on the right side of the UDF affects flapping generated on the right side of the DDF. There appears to be no significant change in velocity distribution or vectors over the (*a*) IDF and (*b*) $S/D = 3$ and (*d*) 5. The result contradicts the observation that, as S/D increases, the flame width of the DDF (W_d) increases. This contradiction can be explained by the fact that the velocity defect region is wider downstream, which in turn causes a broader flame width downstream of the DDF. Therefore, when the burner is positioned downstream of the DDF, the visible area of the flame extends in the spanwise direction. The interface between the red and blue regions is wavy, confirming the effect of flapping. The instability of the interface becomes more pronounced downstream of the DDF. Comparing (*b*) and (*c*), the heat release rate is doubled in (*c*), resulting in a slight increase in cross-wind
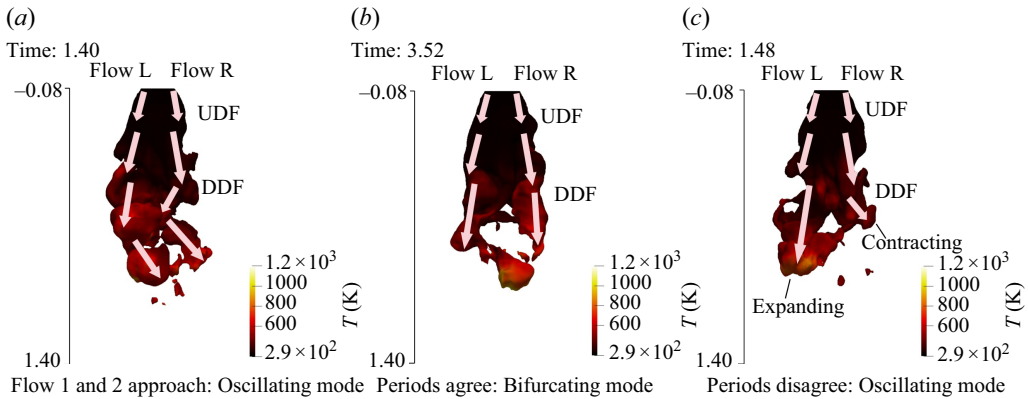
Figure 17. Three types of flapping mechanisms. Numerical conditions are $S/D = 3$, $u_c = 2.0$ m s^{-1}, $\dot{Q}_u = 17.43$ kW and $\dot{Q}_d = 17.43$ kW. See also Movie 3 for the computational video image of flame volume corresponding to $S/D = 3$, $u_c = 2.0$ m s^{-1}, $\dot{Q}_u = 17.43$ kW and $\dot{Q}_d = 17.43$ kW.

velocity around the DDF. This increase may be due to the effect of increased entrainment (see streams (3) and (4) in figure 15), but it also affects the upstream. The slight increase in cross-wind may reduce the flame width of the UDF, but the experimental values (figure 3) do not show this trend.

Figure 17 depicts the three types of flapping mechanisms. When viewed from above, the gas flow near the interface on the left side is referred to as Flow L, and that on the right side is referred to as Flow R. As explained in figure 16, Flow L and Flow R slightly move to the left and right. If Flow L and Flow R merge or are close together and point in the same direction, the system is in the oscillating mode (figure 17a). In contrast, if Flow L and Flow R point in opposite directions, this is the bifurcating mode (figure 17b). Another possibility is that the flame tips on Flow L and Flow R have different lengths (figure 17c). This mode may be difficult to judge because the flame may appear to be both in the oscillating and bifurcating modes, depending on the length of the flame. The safe way to determine the mode is to make it the same as the previous mode. It should be noted that, in the oscillating mode, the flame front at the tip of the flame is oriented in the same direction on both sides, as shown in figure 17(a), and in the opposite direction, as shown in figure 17(c). The difference in flame tip length between the left and right flames is thought to be pulsating due to puffing in the cross-wind direction, depicted as 'Pulsating' in figure 17(c). Pool fires oscillate in the height direction, but this flame oscillates in the cross-wind direction.

Next, we discuss the mechanism of mode switching. Figure 18(a) shows the mechanism of switching from oscillating mode to bifurcating mode, and figure 18(b) shows the mechanism of the switching from bifurcating mode to oscillating mode. In figure 18(a), the centre part of the flame splits into two flames. This is thought to be caused by a difference in the period of the left and right flapping. In figure 18(b), the flame that branched at both ends (5.80 s) is pointing in the same direction at the next instant (5.88 s), indicating a switch to oscillating mode. This switching is also thought to be caused by the difference between the left and right periods of the flapping. The difference between the left and right flapping cycles is thought to cause mode switching.

An increase in cross-wind velocity increases the frequency of flapping (see figure 4). Figure 19 shows the power (m^2) vs frequency f (Hz) by the FFT of the flame length data. The respective conditions are: (a) DDF and $u_c = 1.2$ m s^{-1}, (b) DDF and $u_c = 2.0$ m s^{-1} and (c) DDF and $u_c = 3.0$ m s^{-1}. The burner distance is $S/D = 3$, and $Q_u = 17.43$ kW
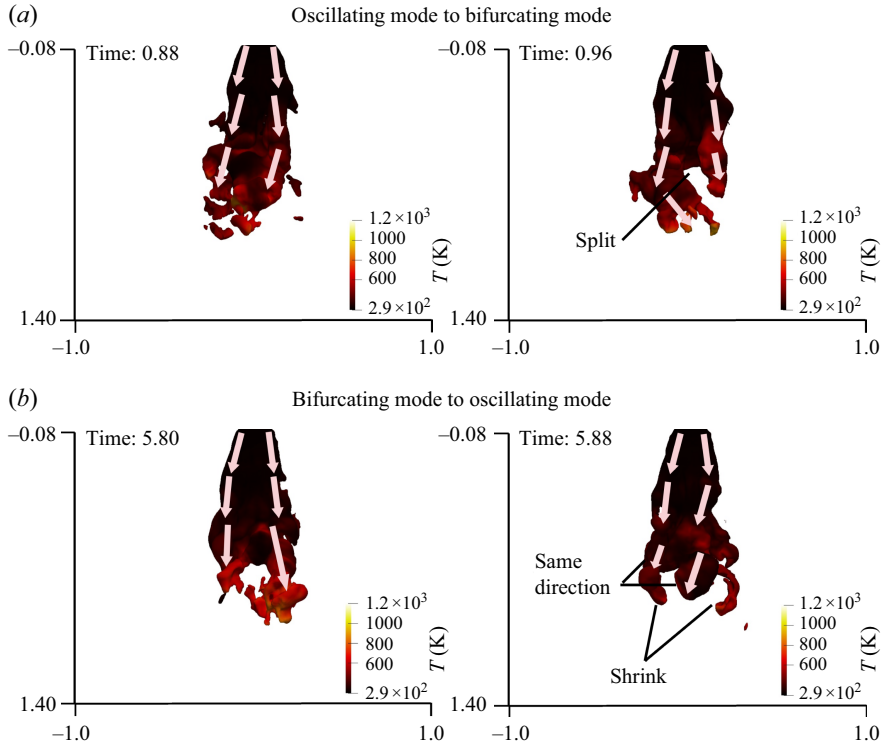
Figure 18. Mode switching mechanisms. Numerical conditions are $S/D = 3$, $u_c = 2.0$ m s^{-1}, $\dot{Q}_u = 17.43$ kW and $\dot{Q}_d = 17.43$ kW.
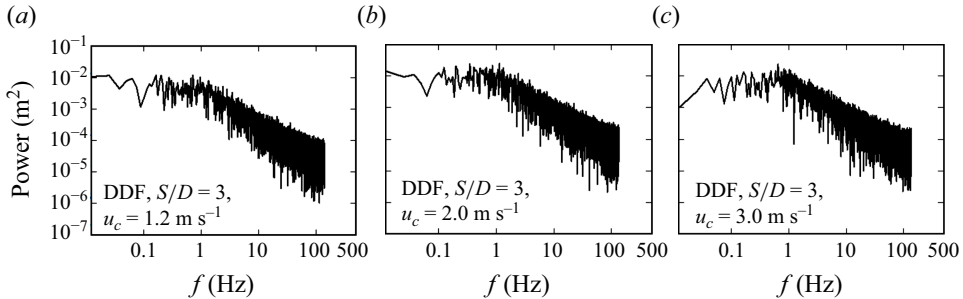

Figure 19. Power (m^2) vs frequency f (Hz) by the FFT of the flame length data, where f is the frequency, f_{max} is the peak frequency and the flame length is determined by the longest coordinate value in the cross-wind direction obtained by the simulations. The results are shown for the following cases: (*a*) DDF and $u_c = 1.2$ m s^{-1}, (*b*) DDF and $u_c = 2.0$ m s^{-1} and (*c*) DDF and $u_c = 3.0$ m s^{-1} with $\dot{Q}_u = 17.43$ kW, $\dot{Q}_d = 17.43$ kW and $S/D = 3$. The power drops approximately at $f = 1$ Hz.

and $Q_d = 17.43$ kW. The flame length is determined by the longest coordinate value in the cross-wind direction obtained by the simulations. The criterion is (3.7), the same as the flame height definition. The power drops approximately at $f = 1$ Hz. The variations in flame length reveal that the energy begins to decay at approximately 1 Hz, regardless of wind speed. This trend indicates that the primary factor of the characteristic frequency of energy dissipation is buoyancy rather than the effects of cross-wind. Concerning flapping frequency (figure 4), at low cross-wind velocity (1.2–2.0 m s^{-1}), the flapping frequency

is closer to puffing, and interaction is more likely to occur. At higher cross-wind velocity (3.0 m s^{-1}), the flapping frequency increases, so the puffing effect is relatively small.

Ultimately, the occurrence of the flapping phenomenon must be discussed based on numerical results. The main cause of the flapping phenomenon is considered to be cross-wind-induced wake. Assuming a representative diameter of 0.15 m, an atmospheric property of 293 K and $u_c = 2.0 \text{ m s}^{-1}$, a Reynolds number ($Re$) is approximately 20,000. The well-known type of wake is the Kármán vortex, which appears behind a cylinder. Kourta *et al.* (1987) reported that velocity deficit regions appeared behind the cylinder for $2{,}000 < Re < 16{,}000$. There is a similarity in that the wake of a cross-wind causes the phenomenon. The next possibility is the puffing phenomenon in buoyant fires, which pulsates vertically. This cross-wind changes the direction of pulsating from vertical to the same direction as the cross-wind, and this pulsation also changes the timing of expansion and contraction of the left and right flames in the direction of the cross-wind. This pulsating phenomenon has been confirmed experimentally and numerically. The last effect that may have some influence is the lifting effect of the flame by the entrainment (streams (3)', (4)' and (2)' in figure 15). These streams may collide with the flame and cause velocity fluctuations in the spanwise direction. However, a slight change in velocity is observed as shown in figure 16, but the effect on flame width is minor.

3.3. *Scaling analysis*

We have investigated this flapping phenomenon both experimentally and computationally. The following is a scaling analysis performed in this section, referring to the results in the previous sections to analyse the maximum width of the DDF in the spanwise direction (W_d). Note that the thermal and chemical effects of the DDF on the UDF are not taken into account because of the separation distance ranging from $S/D = 3$ to 5, where these effects can be neglected. A set of controlling parameters W_d is listed as

$$W_d = f\left(\dot{Q}_u, \dot{Q}_d, \rho_\infty, \rho_{vap}, \Delta\rho, \nu_\infty, C_{p,\infty}, D, T_\infty, \Delta T, g, S, u_c \right), \qquad (3.10)$$

where ρ_∞ and T_∞ are the density and temperature in ambient air, $\Delta\rho$ and ΔT are the difference between the ambient and the flame of density and temperature, $C_{p,\infty}$ is the specific heat in ambient air, ρ_{vap} is the density of fuel vapour and ν_∞ is the kinematic viscosity in ambient air. Applying the Buckingham–π theorem in dimensional analysis to (3.10) yields

$$\Pi_8 = f\left(\Pi_1, \Pi_2, \Pi_3, \Pi_4, \Pi_5, \Pi_6, \Pi_7 \right), \qquad (3.11)$$

where Π_i are the dimensionless parameters: $\Pi_8 = W_d/D$, $\Pi_1 = u_c D/\nu_\infty$, $\Pi_2 = S/D$, $\Pi_3 = \rho_{vap}/\rho_\infty$, $\Pi_4 = \dot{Q}_u/(\rho_\infty C_{p,\infty} T_\infty g^{1/2} D^{5/2}) = \dot{Q}_u^*$, $\Pi_5 = \dot{Q}_d/(\rho_\infty C_{p,\infty} T_\infty g^{1/2} D^{5/2}) = \dot{Q}_d^*$, $\Pi_6 = \Delta\rho/\rho_\infty$ and $\Pi_7 = \Delta T/T_\infty$. Because Π_6 and Π_7 are constants in ordinary fires as suggested in Kuwana *et al.* (2008) and Hartl & Smits (2016). Re-arranging these dimensionless terms, equation (3.11) can be written as

$$\Pi_8 = f(\Pi_1, \Pi_2, \Pi_3, \Pi_4, \Pi_5). \qquad (3.12)$$

Thus, the non-dimensional maximum width of the DDF could be expressed as

$$\frac{W_d}{D} = f\left(\frac{u_c D}{\nu_\infty}, S/D, \dot{Q}_u^*, \dot{Q}_d^*, \frac{\rho_{vap}}{\rho_\infty} \right). \qquad (3.13)$$

Figure 20 shows the physical model of the spanwise flapping in the two modes by combining the above procedures. There are momentum exchanges between the flame and cross-wind due to the flame–cross-wind mixing, influenced by the ambient viscosity. Moreover, this viscosity effect may impact the pressure loss in the wake (Fric & Roshko
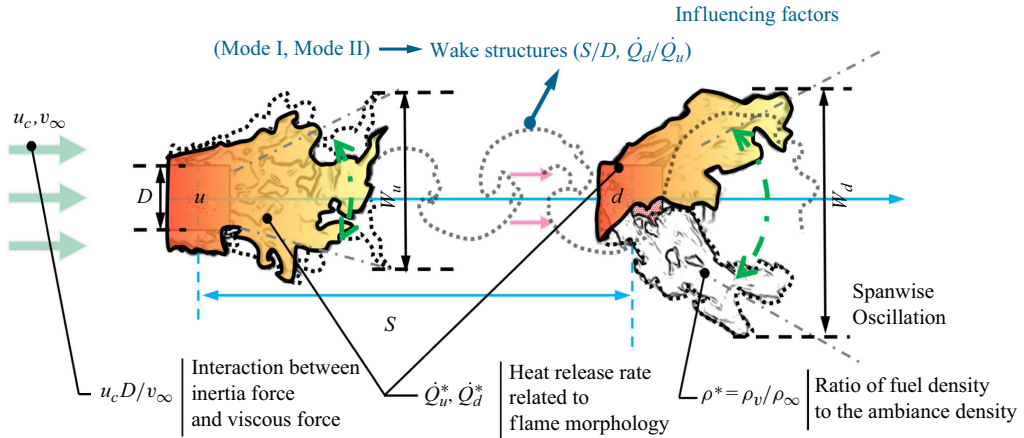
Figure 20. Schematic diagram showing the physics affecting the tandem flame-flapping behaviour under cross-wind in the spanwise direction.

1994). That is, $u_c D/\nu_\infty$ represents the same formula as a Reynolds number, indicating the ratio of cross-wind-induced inertia and ambient viscosity (Zhu 2009). As discussed at the end of § 3.2.3, the cross-wind-induced wake behind the UDF is a significant factor relevant to flame-oscillation and bifurcating phenomena in the spanwise direction (see figures 6, 12 and 16). Moreover, S/D affects the DDF flame width due to wake structures behind the UDF (see figures 6, 12 and 16). $\dot{Q}_d^*/\dot{Q}_u^*$ (equal to $\dot{Q}_d/\dot{Q}_u$) with the same pool size is relevant to the velocity defect regions behind the UDF. For example, the cross-wind velocity ahead and behind the DDF increases for $\dot{Q}_d > \dot{Q}_u$ (see figure 16(b), (c)). Therefore, $\dot{Q}_d/\dot{Q}_u$ also impacts the wake structures behind the UDF (Chen *et al.* 2021). The parameter $\dot{Q}_d^*$ is used as a fundamental parameter to determine flame geometry, such as flame height (Hamins *et al.* 1996) and width (Lei *et al.* 2022a), and hence should be taken into account. The value of ρ_{vap}/ρ_∞ implies the density ratio of gaseous fuel to the ambient fluid, which is also closely associated with the combustion and flame morphological behaviour (Hu *et al.* 2017). This density ratio is relevant to entrainment because the flame drags the surrounding air and supplies the oxidiser due to a difference in density. The occurrence and path of entrainment have already been discussed at the end of § 3.2.3 and in figure 15.

So far, relevant variables related to W_d have been discussed, but the same argument could be applied to the maximum width of the UDF and IDF. However, those are the lack of the effects by S/D and $\dot{Q}_d/\dot{Q}_u$. Their low lateral amplitudes are mainly influenced by the wake flow close to their flame tip region. Thus, W_u and W_i could be expressed as the following functional correlation:

$$\frac{W_{u\,or\,i}}{D} = f\left(\frac{u_c D}{\nu_\infty}, \dot{Q}_{u\,or\,i}^*, \frac{\rho_{vap}}{\rho_\infty}\right). \tag{3.14}$$

The experimental data are then statistically correlated by the proposed scaling law for the UDF, IDF and DDF, as illustrated in figure 21(a), (b), respectively. Based on the least square fit, the best fitting results for those above governing dimensionless parameters are
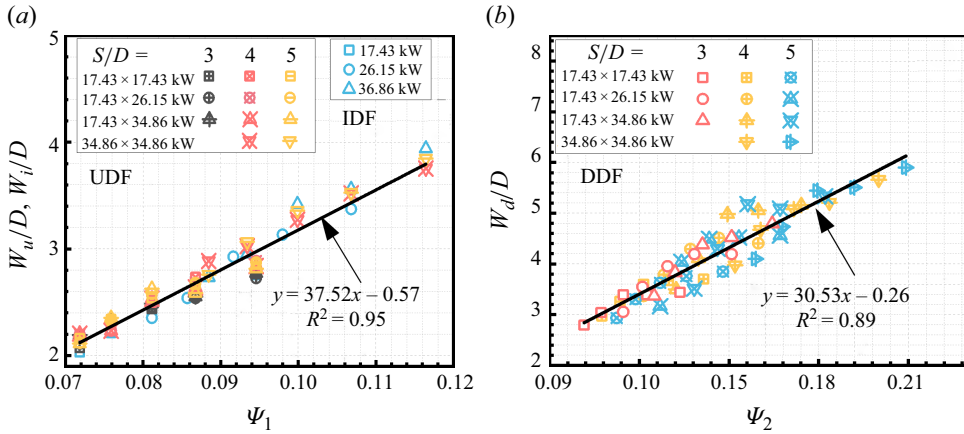
Figure 21. Correlation of non-dimensional spanwise flame amplitude in terms of the proposed dimensionless group based on the physics, (*a*) UDF and IDF; (*b*) DDF.

reasonably represented by piecewise linear functions

$$
\begin{cases}
\dfrac{W_{u\ or\ i}}{D} = 37.52\Psi_1 - 0.57 & 0.072 \leqslant \Psi_1 \leqslant 0.11, \\[2mm]
\dfrac{W_d}{D} = 30.53\Psi_2 - 0.26 & 0.101 \leqslant \Psi_2 \leqslant 0.209,
\end{cases}
\tag{3.15}
$$

where $\Psi_1 = (u_c D/\nu_\infty)^{-0.3} \dot{Q}_{u\ or\ i}^{*0.3} (\rho_{vap}/\rho_\infty)^{0.5}$, $\Psi_2 = (u_c D/\nu_\infty)^{-0.3} \dot{Q}_d^{*0.5} [(S/D)/(\dot{Q}_d^*/\dot{Q}_u^*)]^{0.2} (\rho_{vap}/\rho_\infty)^{0.5} = (u_c D/\nu_\infty)^{-0.3} \dot{Q}_d^{*0.3} [(S/D)\dot{Q}_u^*]^{0.2} (\rho_{vap}/\rho_\infty)^{0.5}$. The negative exponent of $u_c D/\nu_\infty$ indicates that W becomes narrower with increasing u_c, while the positive exponents of S/D, $\dot{Q}_d^*$ and $\dot{Q}_u^*$ signify the positive relationship against W_d, which is consistent with the results shown in figure 6. The unsteady flame–lapping behaviour of both fires in the spanwise direction is substantially characterised by invisible flow structures, as indicated by the oscillating mode and bifurcating mode, which are induced by the interaction between hot flame fluid and cross-wind fluid. Moreover, the wake vortical structure effects on W_d are reflected implicitly through S/D, $\dot{Q}_u^*$ and $u_c D/\nu_\infty$. Note that the analysis mainly focuses on the relatively strong cross-wind ($\geqslant 1.2$ m s^{-1}). Vertical flame thermal buoyancy might mitigate the flame-flapping motion in the spanwise direction when the buoyancy and inertial force are of the same order of magnitude at a smaller u_c.

4. Conclusions

This study experimentally and numerically investigated the flapping behaviour in the spanwise direction of tandem diffusion flames of varying separation distances ($S/D = 3 - 5$) under a strong cross-wind effect. Both instantaneous lateral flame behaviour evolution as a function of time and time-averaged maximum flame width magnitude were quantified and analysed. Simulations following the experimental conditions were performed to understand better the phenomena observed in the experiments. Based on the involved physics, a scaling law was developed to characterise the maximum flame width.

From the observations, two modes of the DDF lateral flapping motion were identified. One was the oscillating mode, for which the downstream flame flapped under the action of the wake vortices of the UDF. Another was the bifurcating mode. Moreover, the flame

Y. Chen, K. Fukumoto, Y. Miao, J. Zheng, F. Tang and L. Hu

alternated between oscillating and bifurcating modes. The movement of the upper and lower edges of the flame was more chaotic for the DDF compared with the UDF. As the cross-wind velocity increased, the amplitudes of the upper and lower edges decreased for both the UDF and DDF. Specifically, the amplitude of the DDF edge at 1.2 m s^{-1} was almost twice that at 3.0 m s^{-1}. These time-averaged maximum flame widths were found to be nearly identical for both the UDF and IDF at the same heat release rate. However, the maximum flame width of the DDF was greater than that of the UDF and increased with increasing S/D due to the UDF's widened and disentangled wake. The maximum flame width of the DDF is nearly 1.6 times that of the UDF when $u_c = 2.0$ m s^{-1}. Frequency analysis of flapping was performed at $S/D = 3$, $u_c = 1.2$–3.0 m s^{-1}, and $\dot{Q}_u^* = \dot{Q}_d^* = 17.43$ kW. The flapping of the UDF was generally around 0.2–1.8 Hz and did not change significantly at 1.2–3.0 m s^{-1}. The flapping of the DDF was generally 0.5–2.2 Hz, with the frequency increasing as the cross-wind velocity increased. The frequency at which the mode switched was approximately 1–3 Hz, with higher frequencies and more frequent mode switching at a higher cross-wind velocity.

Next, our numerical simulation could reproduce both the oscillating mode and the bifurcating mode. Air was supplied by the cross-wind near or far from the fire source with ambient entrainment. The cross-wind near the fire source moved the fires in the cross-wind direction, while the cross-wind far from the fire source lifted them. Entrainment from the surroundings was used to lift the fire near the fire source. All streams and fires merged to form one large plume. Flapping occurred on the left and right sides of the UDF, and the effects of each propagated to the left and right sides of the DDF, respectively. Behind the burner, a region of velocity defects spread downstream. The causes of such flapping were turbulence caused by cross-winds, the puffing phenomenon seen in buoyant fires and collisions between the fires and an updraft generated below them. The misalignment or coincidence of flapping periods causes flapping. When a flame was viewed from the top, it was in the oscillating mode if the left and right flows were facing the same direction. In the bifurcating mode, they were facing the opposite direction. In addition, the flame appeared to be in the oscillating mode when the lengths of the left and right flames differed. In the oscillating mode, a single flame split into two flames, and in the bifurcating mode, the two flames merged. These phenomena occurred due to the difference in the flapping cycles of the left and right flames.

Finally, an attempt was made to conduct a scaling analysis using experimental observations and simulations to explain the flapping mechanism. The scaling analysis identified $u_c D/\nu_\infty$, S/D, $\dot{Q}_{i, u, or, d}^*$ and ρ_{vap}/ρ_∞ as controlling variables, which can be correlated well with the proposed dimensionless groups, regarding the maximum flame width data.

This study provided the underlying knowledge of flapping of tandem diffusion flames in the spanwise direction under cross-wind conditions, which provides the information for determining the distance required for fire safety in scenarios such as fires in adjacent office buildings and houses. Attention to the flame-flapping phenomenon helps prevent the potential hazard of multiple fires.

Supplementary movies. Supplementary movies are available at https://doi.org/10.1017/jfm.2025.10182.

Declaration of interests. The authors report no conflict of interest.

Appendix A. Dynamic Smagorinsky model: incompressible vs compressible versions

A verification study comparing the incompressible and compressible dynamic Smagorinsky models (Moin *et al.* 1991) showed negligible differences in temperature rise and velocity distribution (figure 22), which indicates that the density correction applied to the incompressible model is sufficient for this study. Thus, the incompressible dynamic Smagorinsky model is adopted throughout this study without loss of accuracy.
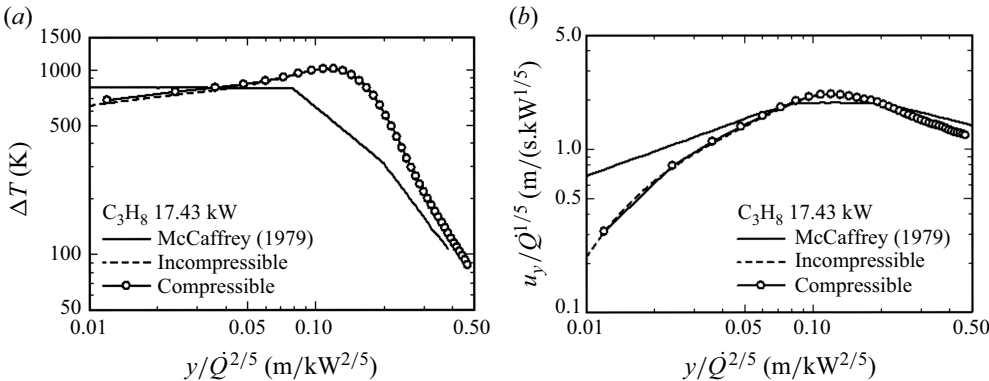

Figure 22. (*a*) Temperature rise and (*b*) normalised velocity vs normalised coordinate using incompressible/compressible dynamic Smagorinsky model.
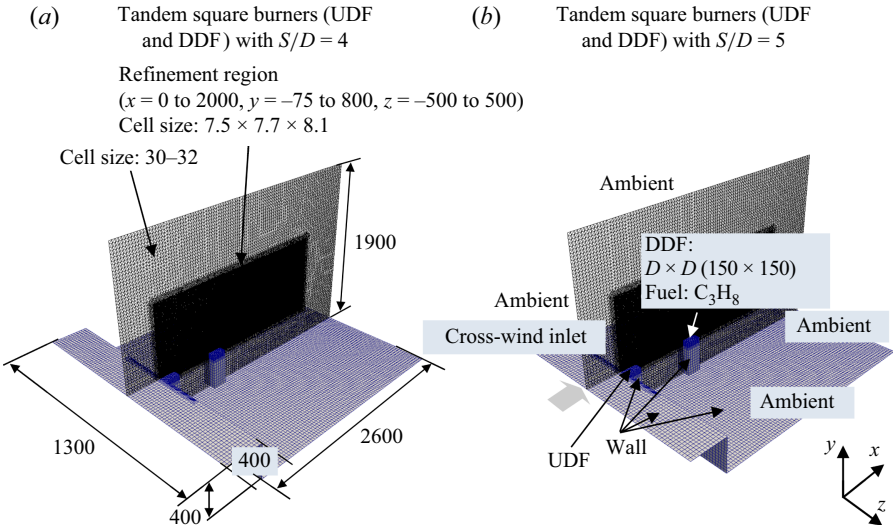

Figure 23. Computational domain for tandem square burners for $S/D = 4$ and $S/D = 5$. Note that the coordinate origin $(0, 0, 0)$ is on the square burner and UDF centres. Bolded texts indicate boundary conditions; see table 1 for each. The unit of length is mm.

Figure 24. (*a*) Computational domain for tandem square burners for $H = 800$ mm and $S/D = 3$. Note that the coordinate origin $(0, 0, 0)$ is on the square burner and UDF centres. Bolded texts indicate boundary conditions; see ta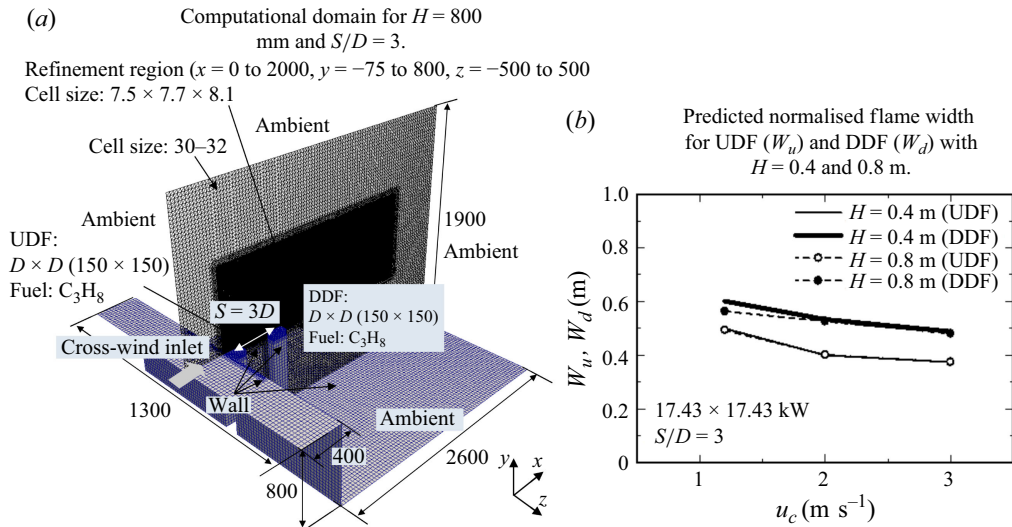ble 1 for each. The unit of length is mm. (*b*) The predicted normalised flame width for the UDF (W_u) and DDF (W_d) corresponding to $S/D = 3$, $u_c = 1.2 \text{ m s}^{-1}$, $\dot{Q}_u = 17.43$ kW and $\dot{Q}_d = 17.43$ kW.

Appendix B. Computational domains with $S/D = 4$ and 5

Figure 23 shows computational meshes and domains with (a) $S/D = 4$ and (b) $S/D = 5$ for tandem square burners, where the names used in figure 23 (e.g. gas burner) for the boundary conditions are consistent in table 1. The burner shape was square with 150×150 mm.

Appendix C. Effect of burner heights

Figure 24 shows (*a*) the computational domain for tandem square burners with $H = 800$ mm and $S/D = 3$ and (*b*) the predicted flame width (W_u, W_d) vs cross-wind velocity u_c at burner heights of 0.4 and 0.8 m, with $S/D = 3$, $\dot{Q}_u^* = 17.34$ kW and $\dot{Q}_d^* = 17.34$ kW. For both burner heights, the flame width decreases with increasing cross-wind velocity u_c, consistent with the entrainment flow being governed by the cross-wind conditions. While the burner height does influence the flame width to some extent, this effect is limited. Notably, for DDF at $u_c = 1.2 \text{ m s}^{-1}$, the flame width is slightly shorter for the taller burner (0.8 m), but the effect is marginal. As the cross-wind velocity increases, the influence of burner height on the flame width becomes less significant. These results support the conclusion that, while the burner height has a slight effect, the cross-wind velocity remains the dominant factor influencing flame behaviour.

REFERENCES

BALDWIN, R. 1968 Flame merging in multiple fires. *Combust. Flame* **12** (4), 318–324.

CETEGEN, B.M. & AHMED, T.A. 1993 Experiments on the periodic instability of buoyant plumes and pool fires. *Combust. Flame* **93** (1-2), 157–184.

CHEN, Y.H., FANG, J., ZHANG, X.L., MIAO, Y., LIN, Y., TU, R. & HU, L.H. 2023a Pool fire dynamics: principles, models and recent advances. *Prog. Energy Combust. Sci.* **95** (101070), 1–54.

CHEN, Y.H., FUKUMOTO, K., ZHANG, X., LIN, Y., TANG, F. & HU, L.H. 2023b Study of elevated- and ground pool fire flame horizontal lengths in cross airflows: air entrainment change due to Coanda effect. *Proc. Combust. Inst.* **39** (3), 4063–4073.

CHEN, Y.H., HU, L.H., KUANG, C., ZHANG, X.L., LIN, Y.J. & ZHONG, X.P. 2021 Flame interaction and tilting behaviour of two tandem adjacent hydrocarbon turbulent diffusion flames in crosswind: an experimental quantification and characterisation. *Fuel* **290** (119930), 1–10.

CHEN, Z., WEN, J.X., XU, B. & DEMBELE, S. 2014 Large eddy simulation of a medium-scale methanol pool fire using the extended eddy dissipation concept. *Intl J. Heat Mass Transfer* **70**, 389–408.

EMORI, R.I. & SAITO, K. 1983 A study of scaling laws in pool and crib fires. *Combust. Sci. Technol.* **31** (5-6), 217–231.

ERTESVÅG, I.S. & MAGNUSSEN, B.F. 2000 The eddy dissipation turbulence energy cascade model. *Combust. Sci. Technol.* **159** (1), 213–235.

FINNEY, M.A. & MCALLISTER, S.S. 2011 A review of fire interactions and mass fires. *J. Combust.* **2011** (1), 1–14.

FRIC, T.F. & ROSHKO, A. 1994 Vortical structure in the wake of a transverse jet. *J. Fluid Mech.* **279**, 1–47.

FUKUMOTO, K., WANG, C.J. & WEN, J.X. 2018 Large eddy simulation of upward flame spread on PMMA walls with a fully coupled fluid-solid approach. *Combust. Flame* **190**, 365–387.

FUKUMOTO, K., WANG, C.J. & WEN, J.X. 2019 Large eddy simulation of a syngas jet flame: effect of preferential diffusion and detailed reaction mechanism. *Energy Fuels* **33** (6), 5561–5581.

FUKUMOTO, K., WEN, J.X., LI, M., DING, Y. & WANG, C. 2020 Numerical simulation of small pool fires incorporating liquid fuel motion. *Combust. Flame* **213**, 441–454.

FUKUMOTO, K., WANG, C.J. & WEN, J.X. 2022 Study on the role of soot and heat fluxes in upward flame spread using a wall-resolved large eddy simulation approach. *J. Therm. Anal. Calorim.* **147** (7), 4645–4665.

GERMANO, M., PIOMELLI, U., MOIN, P. & CABOT, W.H. 1991 A dynamic subgrid-scale eddy viscosity model. *Phys. Fluids* **3** (3), 1760–1765.

GIACOMAZZI, E., PICCHIA, F.R. & ARCIDIACONO, N. 2008 A review of chemical diffusion: criticism and limits of simplified methods for diffusion coefficient calculation. *Combust. Theor. Model.* **12** (1), 135–158.

HAMINS, A., KONISHI, K., BORTHWICK, P. & KASHIWAGI, T. 1996 Global properties of gaseous pool fires. *Symp. (Intl) Combust.* **26** (1), 1429–1436.

HARRIS, S.J. & MCDONALD, N.R. 2022 Fingering instability in wildfire fronts. *J. Fluid Mech.* **943**, 1–26.

HARTL, K.A. & SMITS, A.J. 2016 Scaling of a small scale burner fire whirl. *Combust. Flame* **163**, 202–208.

HESKESTAD, G. 2016 Fire plumes, flame height, and air entrainment. In *SFPE Handbook of Fire Protection Engineering*, 5th edn, chap. 13. Springer.

HU, L.H., ZHANG, X.L., DELICHATSIOS, M.A., WU, L. & KUANG, C. 2017 Pool fire flame base drag behaviour with cross flow in a sub-atmospheric pressure. *Proc. Combust. Inst.* **36** (2), 3105–3112.

JI, J., GE, F.L. & QIU, T.T. 2021 Experimental and theoretical research on flame emissivity and radiative heat flux from heptane pool fires. *Proc. Combust. Inst.* **38** (3), 4877–4885.

KOURTA, A., BOISSON, H.C., CHASSAING, P. & MINH, H.H. 1987 Nonlinear interaction and the transition to turbulence in the wake of a circular cylinder. *J. Fluid Mech.* **181**, 141–161.

KUWANA, K., SEKIMOTO, K., SAITO, K. & WILLIAMS, F.A. 2008 Scaling of a small scale burner fire whirl. *Fire Safety J.* **43** (4), 252–257.

LEE, Y., DELICHATSIOS, M.A. & SILCOCK, G.W.H. 2007 Heat fluxes and flame heights in facades from fires in enclosures of varying geometry. *Proc. Combust. Inst.* **31** (2), 2521–2528.

LEI, J., HUANG, P.C., LIU, N.A. & ZHANG, L.H. 2022*a* On the flame width of turbulent fire whirls. *Combust. Flame* **244**, 112285.

LEI, J., DENG, W.Y., LIU, Z.H., MAO, S.H., SAITO, K., TAO, Y., WU, H.M. & XIE, C.L. 2022*b* Experimental study on burning rates of large-scale hydrocarbon pool fires under controlled wind conditions. *Fire Safety J.* **127**, 103517.

LI, B., DING, L., SIMEONI, A., JI, J., WAN, H. & YU, L. 2021 A numerical investigation of the flow characteristics around two tandem propane fires in a windy environment. *Fuel* **286**, 119344.

LILLY, D.K. 1992 A proposed modification of the Germano subgrid: scale closure method. *Phys. Fluids* **4** (3), 633–633.

LIU, N., LEI, J., GAO, W., CHEN, H. & XIE, X. 2021 Combustion dynamics of large-scale wildfires. *Proc. Combust. Inst.* **38** (1), 157–198.

MAGNUSSEN, B.F. & HJERTAGER, B.H. 1977 On mathematical modeling of turbulent combustion with special emphasis on soot formation and combustion. *Symp. (Intl) Combust* **16** (1), 719–729.

MAGNUSSEN, B.F. 1981 On the structure of turbulence and a generalized eddy dissipation concept for chemical reaction in turbulent flow. In *Proceedings of the 19th Aerospace Sciences Meeting*, *AIAA Paper 81-0042*.

MARAGKOS, G., BEJI, T. & MERCI, B. 2017 Advances in modelling in CFD simulations of turbulent gaseous pool fires. *Combust. Flame* **181**, 22–38.

MARAGKOS, G. & MERCI, B. 2020 On the use of dynamic turbulence modelling in fire applications. *Combust. Flame* **216**, 9–23.

MAYNARD, T., PRINCEVAC, M. & WEISE, D.R. 2016 A study of the flow field surrounding interacting line fires. *J. Combust.* **76**, 1–12.

MAYNARD, T.B. & BUTTA, J.W. 2017 A physical model for flame height intermittency. *Fire Technol.* **54** (1), 135–161.

MCCAFFREY, B.J. 1979 Purely buoyant diffusion flames: some experimental results, Tech. Rep. NBSIR 79-1910. Centre for fire research, National engineering laboratory, National bureau of standards.

MCCAFFREY, B. 1995 Flame height. In *SFPE Handbook of Fire Protection Engineering*, 2nd edn, pp. 2-1–2-8. Society of Fire Protection Engineers and National Fire Protection Association.

MOIN, P., SQUIRES, K., CABOT, W. & LEE, S. 1991 A dynamic subgrid-scale model for compressible turbulence and scalar transport. *Phys. Fluids A* **3** (11), 2746–2757.

MORVAN, D., HOFFMAN, C., REGO, F. & MELL, W. 2011 Numerical simulation of the interaction between two fire fronts in grassland and shrubland. *Fire Safety J.* **46** (8), 469–479.

OpenFOAM v2006 2020, Source codes and documentations. Available at: http://www.openfoam.com/.

PASSALACQUA, A. 2021 The source code of the dynamic Smagorinsky model for OpenFOAM. Available at https://github.com/AlbertoPa.

POLING, B.E., PRAUSNITZ, J.M. & O'CONNELL, J.P. 2001 Thermal conductivity. In *The Properties of Gases and Liquids*. 5th edn, chP. 10.3. McGraw-Hill.

QUINTIER, J.G. 1989 Scaling applications in fire research. *Fire Safety J.* **15** (1), 3–29.

RISTROPH, L. & ZHANG, J. 2008 Anomalous hydrodynamic drafting of interacting flapping flags. *Phys. Rev. Lett.* **101** (19), 194502.

SHELLEY, M.J. & ZHANG, J. 2011 Flapping and bending bodies interacting with fluid flows. *Annu. Rev. Fluid Mech.* **43** (1), 449–465.

SHINOHARA, M. & KUDO, K. 2004 Experimental study of the flow structure including whirlwinds in the wake region of a flame in a cross-wind. In *Proceedings of the 6th Asia-Oceania Symposium on Fire Science and Technology*, pp. 120–131. International Association for Fire Safety Science.

SHINTANI, Y., NAGAOKA, T., DEGUCHI, Y., IDO, K. & HARADA, K. 2014 Simple method to predict downward heat flux from flame to floor. *Fire Sci. Technol.* **33** (1), 17–34.

SMAGORINSKY, J. 1963 General circulation experiments with the primitive equations: I. The basic experiment. *Mon. Weath. Rev.* **91** (3), 99–164.

SMOOKE, M.D. 1991 Reduced kinetics mechanisms and asymptotic approximations for methane-air flames. In *Lecture Notes in Physics*, chap. 1. Springer-Verlag.

SMITH, T.F., SHEN, Z.F. & FRLEDMAN, J.N. 1982 Evaluation of coefficients for the weighted sum of gray gases model. *J. Heat Mass Transfer* **104** (4), 602–608.

SUN, Y., LIU, N.A., GAO, W., XIE, X.D. & ZHANG, L.H. 2021 Experimental study on the combustion characteristics of rectangular fire plumes. *Fire Safety J.* **126**, 103477.

TANG, F., DENG, L., HE, Q. & ZHANG, J. 2023 Mass burning rate and merging behaviour of double liquid pool fires under cross winds. *Proc. Combust. Inst.* **39** (3), 4041–4052.

TRELLES, J. & PAGNI, P.J. 1991 Fire-induced winds in the 20 October 1991 Oakland hills fire. *Fire Safety Sci.* **5**, 911–922.

UDDIN, E., HUANG, W.X. & SUNG, H.J. 2015 Actively flapping tandem flexible flags in a viscous flow. *J. Fluid Mech.* **780**, 120–142.

VASANTH, S., TAUSEEF, S.M., ABBASI, T. & ABBASI, S.A. 2014 Multiple pool fires: occurrence, simulation, modeling and management. *J. Loss Prev. Process. Ind.* **29**, 103–121.

WANG, C.J., WEN, J.X. & CHEN, Z.B. 2014*a* Simulation of large-scale LNG pool fires using firefoam. *Combust. Sci. Technol.* **186** (10-11), 1632–1649.

WANG, C.J., WEN, J.X., CHEN, Z.B. & DEMBELE, S. 2014b Predicting radiative characteristics of hydrogen and hydrogen/methane jet fires using firefoam. *Intl J. Hydrogen Energy* **39** (35), 20560–20569.

WHITE, J.P. 2015 Radiative emissions measurements from a buoyant, turbulent line flame under oxidizer-dilution quenching conditions. *Fire Safety J.* **76**, 74–84.

XIA, X. & ZHANG, P. 2018 A vortex-dynamical scaling theory for flickering buoyant diffusion flames. *J. Fluid Mech.* **855**, 1156–1169.

YANG, W. & BLASIAK, W. 2005 Numerical study of fuel temperature influence on single gas jet combustion in highly preheated and oxygen deficient air. *Energy* **30** (2-4), 385–398.

ZHOU, R. & WU, Z.N. 2007 Fire whirls due to surrounding flame sources and the influence of the rotation speed on the flame height. *J. Fluid Mech.* **583**, 313–345.

ZHU, L.D. 2009 Interaction of two tandem deformable bodies in a viscous incompressible flow. *J. Fluid Mech.* **635**, 455–475.

ZUKOSKI, E.E., CETEGEN, B.M. & KUBOTA, T. 1985 Visible structure of buoyant diffusion flames. *Proc. Combust. Inst.* **20** (1), 361–366.